



Tuning the Nanotopography and Chemical Functionality of 3D Printed Scaffolds through Cellulose Nanocrystal Coatings

Mouhanad Babi, Roberto Riesco, Louisa Boyer, Ayodele Fatona, Angelo Accardo, Laurent Malaquin, Jose Moran-Mirabal

► To cite this version:

Mouhanad Babi, Roberto Riesco, Louisa Boyer, Ayodele Fatona, Angelo Accardo, et al.. Tuning the Nanotopography and Chemical Functionality of 3D Printed Scaffolds through Cellulose Nanocrystal Coatings. *ACS Applied Bio Materials*, 2021, 4 (12), pp.8443-8455. 10.1021/acsabm.1c00970 . hal-03547189

HAL Id: hal-03547189

<https://laas.hal.science/hal-03547189>

Submitted on 1 Apr 2022

HAL is a multi-disciplinary open access archive for the deposit and dissemination of scientific research documents, whether they are published or not. The documents may come from teaching and research institutions in France or abroad, or from public or private research centers.

L'archive ouverte pluridisciplinaire **HAL**, est destinée au dépôt et à la diffusion de documents scientifiques de niveau recherche, publiés ou non, émanant des établissements d'enseignement et de recherche français ou étrangers, des laboratoires publics ou privés.

Tuning the nanotopography and functionality of 3D-printed scaffolds for cell culture through tunable cellulose nanocrystal coatings

Mouhanad Babi¹, Roberto Riesco², Louisa Boyer², Ayodele Fatona¹, Angelo Accardo³, Laurent Malaquin² and Jose Moran-Mirabal^{1*}

¹Department of Chemistry and Chemical Biology, McMaster University, Hamilton, Ontario, Canada, L8S 4L8

²LAAS-CNRS, Université Toulouse III - Paul Sabatier, 31400 Toulouse, France

³Department of Precision and Microsystems Engineering, Delft University of Technology, Mekelweg 2, 2628 CD Delft, Netherlands

ABSTRACT

Living cells naturally exist in three-dimensional microenvironments with geometries, topography, stiffness, surface chemistry and biological factors that strongly dictate their phenotype and behaviour. The cellular microenvironment is an organized structure or scaffold that, together with the cells that live within it, make up living tissue. In order to mimic these systems and understand how the different properties of a scaffold influence cell behaviour, such as adhesion, proliferation or function, we need to be able to fabricate cellular microenvironments with tunable properties. In this work, the nanotopography and functionality of scaffolds for cell culture were modified by coating 3D printed materials (DS3000 and PEG-DA) with cellulose nanocrystals (CNCs). This general approach was demonstrated on a variety of structures designed to incorporate macro and microscale features fabricated using photopolymerization 3D printing techniques. Atomic force microscopy was used to characterize the CNC coatings and showed the ability to tune their density and in turn the surface nano-roughening, from isolated nanoparticles to dense surface coverage. The ability to tune the density of CNCs on 3D printed structures could be leveraged to control the attachment and morphology of prostate cancer cells. It was also possible to introduce functionalization onto the surface of these scaffolds, either by directly coating them with CNCs grafted with the functionality of interest, or with a more general approach of functionalizing the CNCs after coating using biotin-streptavidin coupling. The ability to carefully tune the nanostructure and functionalization of different 3D-printable materials is a step forward to creating *in vitro* scaffolds that mimic the nanoscale features of natural microenvironments, which are key to understanding their impact on cells and to develop artificial tissues.

1. INTRODUCTION

The recent advances in 3D printing technologies and biomaterials have given rise to a variety of scaffold designs and compositions designed to mimic natural microenvironments and culture cells *in vitro*. Examples of this include the fabrication of artificial bone grafts through fused deposition modeling of composite calcium phosphate and collagen, extrusion-photopolymerization printing of PEG-DA/alginate hydrogel composites, and electrohydrodynamic jet printing of PCL/PVP scaffolds.¹⁻³ In addition to incorporating a variety of complex geometrical features, these materials present a wide range of mechanical, physical and chemical properties. These differences reflect the desire to mimic cellular niches that are found within the various types of tissues that make up multicellular organisms. While artificial scaffolds are effective in producing bulk 3D structures to encapsulate and support cells, they often still require tuning and functionalization in order to accurately mimic the extracellular matrix

(ECM) features found in real tissue. Whether we would like to understand the role of the ECM on cellular behaviour, study cells in their native environment or create artificial tissue, it is important to be able to fabricate 3D cellular scaffolds with properties similar to those of tissue. This includes micro- to nanoscale features of the ECM, such as topography, stiffness and decoration with various biochemical motifs that all play an important role in the proliferation, migration, differentiation and overall function of the cell.

The *in vivo* extracellular environment possesses nanoscale structures and topography that play a key role in determining the behaviour and function of cells. The main structural component of tissue, the ECM, provides biochemical and mechanical support to cells by virtue of a fibrous network, primarily composed of proteins like collagen and elastin, which possesses nanoscale dimensions and imparts nanotopography within the cellular microenvironment. This fibrous network provides structural and mechanical cues that direct cellular adhesion, morphology, migration and differentiation.^{4–6} For instance, collagen fibrils, which have width of 20 – 200 nm and possess a periodic ridged structure with 67 nm spacings and 5-15 nm grooves, present nanostructures for cells to interact with through integrin-mediated focal or 3D-matrix adhesions.^{7–9} Through these contact points, alignment of collagen fibrils has been shown to guide the migration of fibroblast, epithelial and carcinoma cells within a three-dimensional matrix.^{10–12} *In vivo* substratum nanotopography can also be found in endothelial and corneal epithelium basement membranes, which present a 3D fibrous texture rich of nanoscale (20 - 200 nm) pores and ridges that are vital for cellular adhesion and act as the foundation of the large-scale multicellular architectures including tissues and organs.^{13–15} Given the ubiquitous presence and importance of nanoscale topography *in vivo*, the incorporation of surface nanostructure and roughness during the fabrication of artificial microenvironments is essential to promote relevant behaviour and function of cells cultured *in vitro*.

Nanostructured surfaces can be created using various fabrication and patterning techniques and have been shown to modulate cellular behaviour. Ordered and regular nanoscale features, such as nanopillars, nanogrooves and nanopits, can be achieved using colloidal, electron beam or soft lithography.^{16–18} Merely from the anisotropic topography presented by nanogrooves (320 – 2100 nm wide), human corneal cells elongate and align themselves with the patterns, and in the case of human embryonic stem cells, also differentiate into neuronal lineages without the use of any biochemical differentiation factors.^{17,18,19} Electrospinning of synthetic or natural materials can be used to create highly porous 3D networks of fibers with controllable widths and pores in the sub-micron scale, and have been used to study human ligament fibroblast alignment and proliferation.²⁰ In a bench top fabrication approach, thin films can be wrinkled to produce micro/nanostructured surfaces when deposited on shrinkable substrates. Structuring silicon dioxide through this method was shown to alter the morphology of cultured murine macrophages into star-shaped cells that displayed enhanced phagocytic abilities.²¹ It is clear that incorporating nanoscale structures in artificial scaffolds can play a pivotal role in cell phenotype. However, despite the abundance of nanostructuring techniques, they are often limited to transforming flat surfaces into more complex 2.5D structures or 3D scaffolds with limited depth. While these structures are a significant improvement on commonly used 2D cell culture dishes, they still fall short in encapsulating the complexity present within the 3D environment of biological systems.

Light assisted 3D printing techniques have become an attractive route for the fabrication of cell and tissue culture scaffolds. These techniques use inks containing photo-sensitive resins and initiators that

result in crosslinking when exposed to light either through a projected image or a scanned laser source. By translating the sample or the illuminating light, a 3D structure can be printed layer by layer or pixel by pixel. This additive manufacturing technology allows the fabrication of cellular scaffolds with complex architectures and precisely defined geometries from the macro to the microscopic scale. While the resolution offered by light-assisted 3D-printing is superior to other 3D-printing techniques, the natural diffraction of light limits it to ~200 nm and prevents nanoscale features from being printed onto cellular scaffolds.²² As a result, 3D-printed scaffolds are often smooth and require subsequent modifications to incorporate surface nanostructures.

A way to incorporate nanotopography on the surface of 3D scaffolds is to modify the bulk material with nanoparticles (NPs). Their high surface-area-to-volume ratio makes them easily dispersible and ideal to blend with other materials through bulk mixing or surface coating. Attractive properties of NPs, such as piezoelectricity (TiO_2), magnetism (Fe_3O_4), conductivity (carbon nanotubes), antimicrobial effects (Ag) and biodegradability (nanocellulose) can be imparted to the scaffold with the added benefit of mechanical reinforcement. Their nanometric dimensions also increase the roughness of scaffolds and modify the way cells interact with them. For example, the incorporation of carbon nanotubes, PLGA, hydroxyapatite and silica nanoparticles with 3D scaffolds has been previously shown to enhance the adhesion and proliferation of stem cells, and promote their differentiation to adipogenic, osteogenic and neurogenic lineages.^{23–27} Yet, in most cases the NPs are incorporated within the bulk material before or during fabrication of the 3D scaffolds, which limits their availability on the surface and changes the bulk mechanical properties of the whole scaffold.²⁸ Another challenge for their incorporation into 3D printing inks is that NPs can hinder the photopolymerization of the inks, due to the significant light scattering that they introduce. Given the difficulty in modifying the surface roughness of 3D printed scaffolds, it is not surprising that few studies have quantitatively characterized the nanotopography of composite scaffolds and its impact on cellular adhesion and morphology. A simple method of modifying the surface of 3D-printed scaffolds through NP coatings could thus significantly aid in the study of how nanotopography can impact the behaviour of cells cultured in artificial 3D microenvironments.

In this work, we develop a simple and versatile method (Figure 1) for tuning the nanotopography and functionality of 3D-printed cellular scaffolds through dip-coating with cellulose nanocrystals (CNCs). CNCs are needle-shaped, rigid, and highly crystalline nanoparticles produced through the cleavage of cellulosic materials by strong acid hydrolysis.²⁹ CNCs have lengths of 100 – 200 nm and widths of 5 – 20 nm,³⁰ excellent mechanical properties, and high thermal and chemical stability.³¹ The abundant hydroxyl groups present on the surface of CNCs can be used to graft small molecules or polymers, endowing them with targeted functionalities; to this end, a variety of surface modification approaches have been reported in the literature.^{32–35} Their intrinsic physicochemical properties, biocompatibility, biodegradability and low production cost have made CNCs attractive materials to incorporate into scaffolds for applications in tissue engineering and regenerative medicine.^{36,37}

We have leveraged the intrinsic surface charge of CNCs produced through sulphuric acid hydrolysis to coat 3D printed structures via a layer-by-layer (LbL) dip-coating approach, which relies on a cationic polymer to electrostatically bind CNCs to the surface.³⁸ Such LbL method has been previously used to coat 2D surfaces to produce thin CNC films for biosensing, optical, drug delivery and controlled adhesion applications but to our knowledge has not been used to coat 3D structures or to confer nanotopography and modulate cellular behaviour.³⁹ Our simple and versatile approach is demonstrated on thin-films, 2.5D and 3D structures fabricated from commercially available resins using photopolymerization 3D-

printing. We showcase the ability to tune the nanoroughness and coating density on the 3D printed scaffolds by characterizing the coatings through atomic force microscopy (AFM) and confocal microscopy. The functionalization of the scaffolds with chemically modified CNCs is also demonstrated using two approaches: i) pre-coating functionalization, where the molecule of interest is first grafted onto CNCs and then the functionality is transferred to the scaffold surface during coating; ii) post-coating functionalization, where the scaffold is first coated with functional CNCs and then a second molecule of interest is specifically bound to the CNCs on the scaffold surface. The impact of CNC coatings and their density on the adhesion and morphology of PC3 prostate cancer cells is evaluated to understand how tuneable nanoroughness and surface chemistry can be used to influence cell phenotype. We anticipate that this simple method for tuning the nanotopography and functionality of 3D-printed scaffolds, will aid in the development of biomimetic cellular microenvironments for applications in tissue engineering and regenerative medicine.

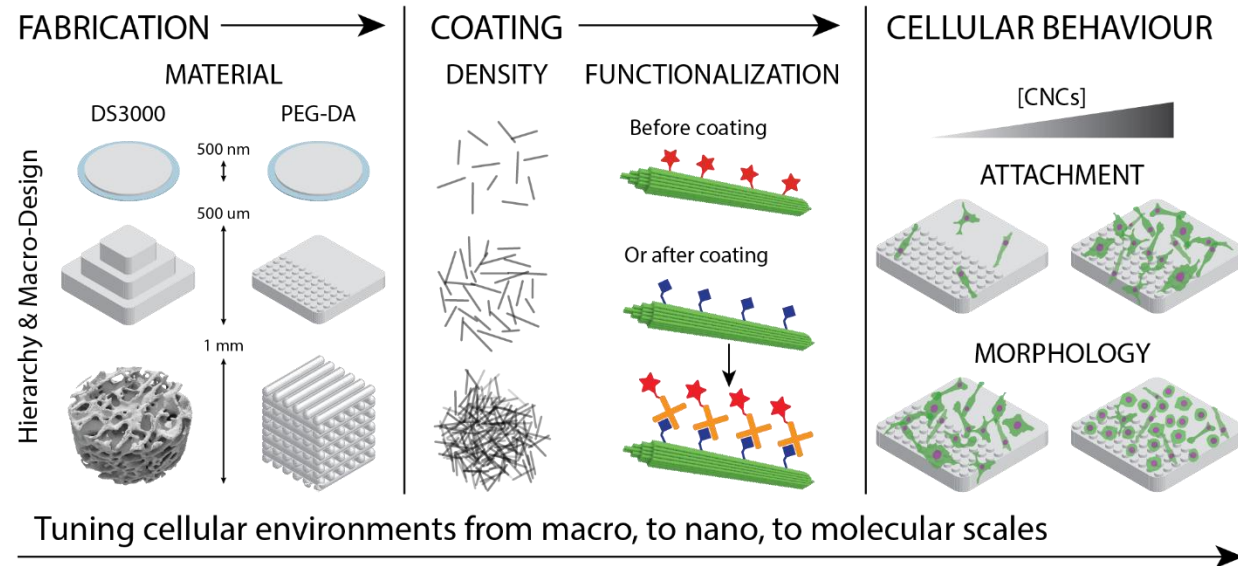


Figure 1. Creating cellular microenvironments with tuneable nanotopography and functionality. Using spin-coating and photopolymerization 3D-printing, cellular scaffolds can be fabricated with increasing complexity from 2D thin films, to 2.5D and 3D structures with geometrical control at the macro- and microscale. The nanostructure of these scaffolds can be finely tuned by a coat of CNCs with a density that can span from sparse to dense coverage of the surface. Using chemically modified CNCs, the scaffold surface can be functionalized during coating with a molecule of interest that is directly grafted onto the CNC surface, or after coating with a molecule that targets the functionality encoded onto the coated CNCs. Careful tuning of the CNC coating density on the 3D-printed scaffolds permits control of cell adhesion and phenotype.

2. RESULTS & DISCUSSION

2.1 Fabrication of cellular scaffolds via 3D-printing

To investigate the ability of the LbL method to coat 3D-printed structures with CNCs, scaffolds of various sizes and geometrical complexities were fabricated using two photosensitive materials with contrasting properties: i) PEG-DA, a polymeric material that is hydrophilic, protein-repellent, and relatively soft (under the fabrication conditions and fully hydrated), and ii) DS3000, a material that is hydrophobic, protein-binding and mechanically stiff. DS3000 was 3D-printed using a single-photon

polymerization stereolithography printer (DWS 028J+, DWS Systems, Italy), which allowed the rapid fabrication of centimeter size structures, with resolutions down to 30 – 40 μm . On the other hand, a two-photon polymerization 3D printing system (Photonic Professional GT, Nanoscribe, Germany) was used to print PEG-DA structures with sub-micron resolution but was limited to sub-millimetre sized designs. PEG-DA scaffolds were printed on glass substrates spin-coated with a thin film of DS3000 to improve adhesion. Thin films of PEG-DA and DS3000 were also used as flat, 2D surfaces to accurately characterize CNC coatings with AFM. This surface characterization was extended to simple 2.5D structures that possessed planar facets compatible with AFM imaging, which included a 300 $\mu\text{m} \times$ 300 $\mu\text{m} \times$ 15 μm base of PEG-DA half-covered with 5 μm diameter, 5 μm high pillars, or DS3000 square pyramids with 700 μm , 500 μm and 300 μm bases (Figure 2A). Coating was then tested on 3D structures that possessed overhanging features, such as the 270 $\mu\text{m} \times$ 270 $\mu\text{m} \times$ 20 μm PEG-DA woodpile and a complex, centimeter sized DS3000 scaffold with a design reconstructed from 3D tomography of horse trabecular bone. Thus, 2D, 2.5D and 3D structures with macroscopic and microscopic features were fabricated from PEG-DA and DS3000 through spin coating, single-photon and two-photon polymerization 3D-printing, and were subsequently used to study the ability to coat these scaffolds with CNCs.

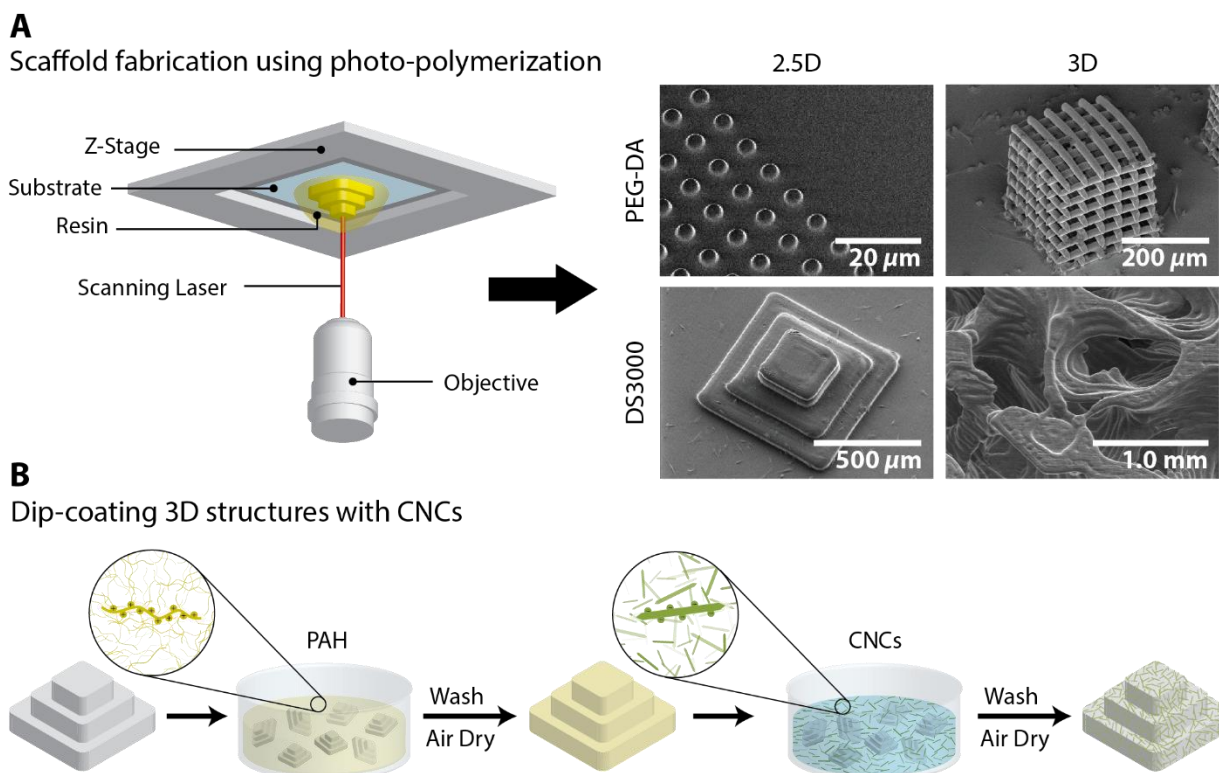


Figure 2. Printing and dip-coating of 3D scaffolds. A) 2.5D and 3D structures made of PEG-DA (MW 700) and DS3000, were fabricated using single-photon and two-photon polymerization 3D-printing. This technique involves a moveable laser source that polymerizes the resin and prints the structure in a layer-by-layer fashion. **B)** Thin-films and 3D-printed structures were coated with CNCs using a layer-by-layer dip-coating approach, which uses the linear cationic polymer PAH as an adhesive layer to bind anionic CNCs to the surface of the structures.

2.2 Coating 3D-printed scaffolds with CNCs to tuneable degrees

Using the LbL dip-coating method, thin-films and 3D-printed structures of DS3000 and PEG-DA were coated with CNCs. Because of the hydrophobic character of the DS3000 samples, samples with 2.5D and 3D structures were first activated with air plasma to increase the surface wettability and avoid the formation of air pockets that could decrease the coating efficiency. The samples were then immersed in a bath containing PAH, a linear polycation, which adsorbed onto the surface and introduced positive charges (Figure 2B). After washing away excess PAH, the structures were placed into a bath containing a suspension of CNCs, which electrostatically bound to the PAH adhesive layer and effectively coated the scaffold surface. The importance of the role played by PAH in coating surfaces with CNCs can be seen by the inability to adsorb any nanoparticles onto PEG-DA thin films when a high concentration of CNCs was used without an initial PAH coating step (Supp. Figure 1A). Furthermore, a 2-step washing of the PAH coated structures was essential to remove excess or loosely bound polymer and obtain uniform and reproducible coatings. Inadequate removal of excess PAH polymer through a single washing step resulted in large voids of CNCs when low coating concentrations were used or led to the formation of a dense, fibrillated cellulose film at high CNC coating concentrations (Supp. Figure 1A and Supp. Figure 2A). In the case of 3D PEG-DA woodpile structures, incomplete washing of PAH caused clogging, webbing and bridging of the scaffolds with cellulose films (Supp. Figure 1B). By thoroughly washing excess PAH, it was possible to reproducibly coat thin films and 3D-printed structures with various concentrations of CNCs.

AFM was used to characterize the surface of coated thin films and 2.5D structures, where the coating density and surface roughness were evaluated as a function of plasma activation and the CNC concentration used during the coating process. For DS3000 thin films coated without plasma activation and a low CNC concentration (3 ppm), the surface was sparsely covered with individual CNCs, and the RMS surface roughness increased from 0.4 nm to 1.0 nm (Figures 3A and 3B). At a 10-fold higher concentration of 30 ppm, the coating density significantly increased and yielded a connected network of CNCs with a roughness of 2.1 nm. This effect leveled off at higher CNC concentrations, with more complete coverage of the thin film and a roughness peak of 2.2 nm (at 300 ppm CNCs) and slight decrease to 1.8 nm when a 3000 ppm CNC solution was used. The decrease in RMS roughness at higher concentrations is attributed to the formation of a complete CNC layer where the roughness is no longer dictated by the difference in height between the diameter of the nanoparticles and the surface, but by the packing between the CNCs themselves, as evidenced by line scans obtained from AFM measurements (Supp. Figure 2B). The coating of PEG-DA thin films yielded similar results with low concentrations resulting in sparse coatings and high concentrations leading to complete surface coverage with CNCs (Supp. Figure 2C).

The dip-coating approach also allowed the controlled deposition of CNC coatings with tuneable density on structures made through 3D-printing from DS3000 and PEG-DA inks (Figure 3A). Unlike spin-coated flat films, which had an RMS roughness of 0.4 nm (Supp. Figure 1A), the surface of 2.5D structures presented inherent topographies stemming from the 3D-printing process or caused by drying and wrinkling. Thus, the RMS roughness of uncoated surfaces varied from 0.5 – 4.0 nm, making it necessary to perform a polynomial background subtraction in order to determine the roughness introduced by the CNC coating (Supp. Figure 3). Surprisingly, the observed roughness of coated 2.5D structures was significantly lower than that of thin films (Figure 3B). This can be seen when comparing the height profiles of CNCs imaged on a DS3000 thin film, which were 4 – 6 nm high, to those on a PEG-DA 2.5D structure which had a height of 2 – 4 nm (Supp. Figure 3). The observed discrepancy could stem

from the inability of the AFM to map the full height of CNCs when they are overlaid on large scale topography or from an over-smoothing by the polynomial fit. The coating efficiency, as visualized from the density of surface bound CNCs, was similar for both thin-films and the PEG-DA 2.5D structures. However, the 2.5D DS3000 pyramid was coated more efficiently, which can be seen by the higher coating density when a dilute CNC solution of 3 ppm was used. This can be explained by the activation of the surface with plasma, which introduces negative surface charges and enhances the adsorption of the positively charged PAH polymer chains. The higher coating efficiency introduced by plasma activation caused the peak in roughness and complete coverage of the surface to occur at more dilute CNC concentrations (Figure 3B). Finally, to demonstrate the ability of this method to uniformly coat microscale features, an AFM scan was acquired from a 5 μm diameter PEG-DA pillar that was coated using a 30 ppm CNC suspension (Figure 3A, bottom row). Through the amplitude error map, it is possible to see homogeneous coverage by CNCs across the base, walls, and top surfaces of the pillar. Altogether, these results show that the dip-coating process allows easily tuning the roughness and density of CNCs on thin films and 3D printed structures made from DS3000 and PEG-DA by simply changing the CNC concentration used.

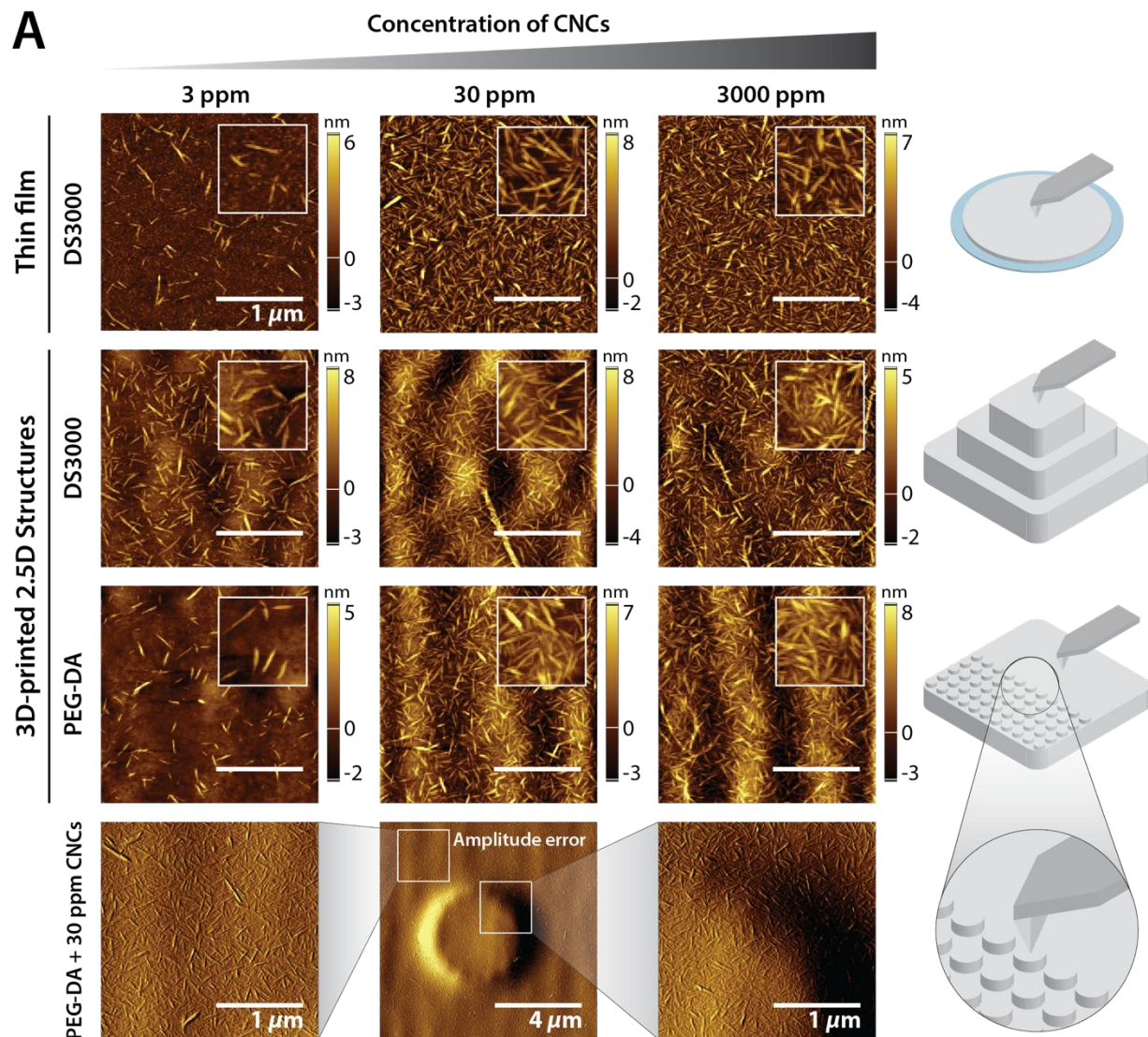
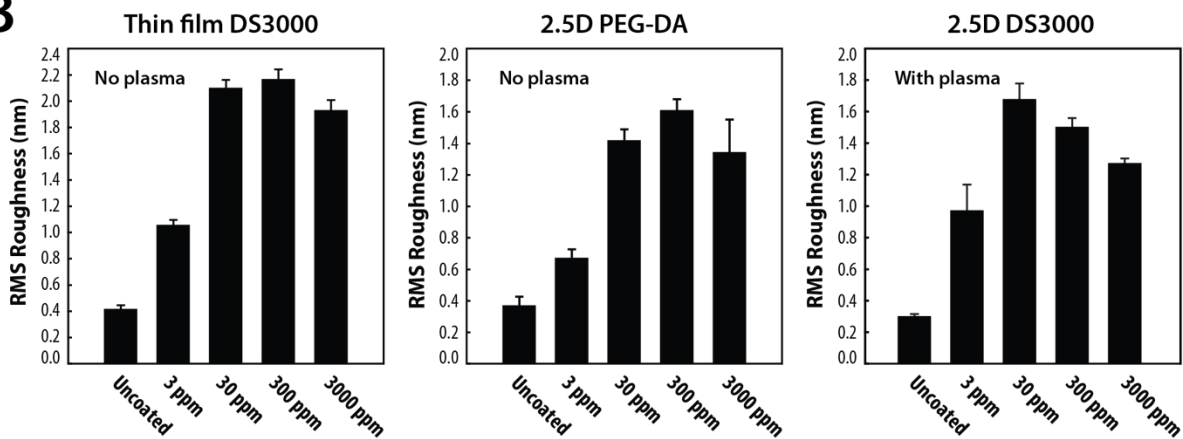
A**B**

Figure 3. Characterization of the CNC coating density using AFM. 2D thin films and 2.5D structures made from PEG-DA and DS3000 were coated with CNCs using suspensions with concentrations of 3, 30 and 3000 ppm. As opposed to the DS3000 pyramid, the DS3000 thin-film and PEG-DA pillars were not activated with plasma before

coating. The resulting surface density and RMS roughness was characterized with AFM, where the tip was positioned on at least three random points on the thin film, the top surface of the DS3000 pyramid or the flat half of PEG-DA pillars. The image insets are a $0.5\text{ }\mu\text{m} \times 0.5\text{ }\mu\text{m}$ portion of the image. RMS roughness was calculated from at least three images, and in the case of 2.5D structures, polynomial background subtraction of the underlying large order topography was performed beforehand. An amplitude error map of a scan of the PEG-DA pillar was generated to highlight the ability to uniformly coat the wall and top surfaces of 3D-printed structures.

2.3 Functionalization of 3D-printed scaffolds with chemically modified CNCs

The use of chemically modified CNCs opens the door to a simple route for the functionalization of 3D-printed scaffolds via dip coating. Through chemical derivatization of CNCs, functionalities of interest can be grafted onto their surface using two strategies: i) pre-coating functionalization, where the moiety of interest is first grafted onto the CNC and later transferred to the scaffold surface during coating, or ii) post-coating functionalization, where the scaffold is first coated with CNCs grafted with a binding moiety and then a second molecule of interest is specifically targeted to the CNCs on the scaffold surface. (Figure 4). The pre-coating functionalization was demonstrated by coating PEG-DA woodpile and DS3000 bone 3D scaffolds with CNCs grafted with the far-red dye Cy5, which allowed their visualization with laser scanning confocal microscopy. With as little as 30 ppm CNCs, 10% of which were grafted with Cy5 dye, the PEG-DA woodpile scaffold displayed a fluorescent coating (Figure 4A, Supp. Figure 4A). At a higher concentration of 3000 ppm CNCs, the full, hollow structure of the beams was easily visible in the orthogonal projections and 3D rendering (Figure 4A, Supp. Figure 4A) of images acquired by confocal microscopy. Coating a trabecular bone scaffold, made from DS3000 resin, with Cy5-CNCs allowed the visualization of the highly complex architecture of the reconstructed bone and demonstrated the ability to coat and functionalize small, free-standing features within the structure (Supp. Figure 4B) using as little as a 3 ppm suspension of Cy5-CNCs. However, due to the heterogeneity in features presented by the scaffold, it was not possible to consistently visualize similar areas within individual prints and study impact of CNC concentration or other conditions on coating.

The post-coating functionalization approach was demonstrated by first coating the scaffolds with CNCs, 10% of which had biotin grafted onto their surface, and then incubating the coated scaffolds with a solution containing Cy5-labeled streptavidin. Functionalization of the structures after coating with Cy5-Streptavidin yielded fluorescence images similar to those obtained with the pre-functionalization approach (Figure 4B), but with lower fluorescence intensity. This was attributed to differences in the degree of functionalization of the CNCs and streptavidin with Cy5. With both functionalization scenarios, it was only possible to visualize the first two layers of the woodpile structure due to limitations to how deep the confocal laser could penetrate (typically $40\text{ }\mu\text{m}$), and how much of the emitted fluorescence could be recorded. However, in cases where the scaffolds were partially detached from the glass substrate, it was possible to acquire an image of the tilted structure and visualize the outer beams of the whole woodpile, which confirmed that the CNC coating was uniform across the whole structure (Supplemental Figure 3B). Through the use of chemically-modified CNCs, it was possible to functionalize 3D scaffolds with Cy5 dyes either through direct functionalization of the through CNCs or streptavidin-biotin coupling. The latter is amenable to a variety of commercially available functionalities that are biologically relevant, such as structural proteins, enzymes, receptors and differentiation factors which are key members of cellular microenvironments found in tissues. Functionalization through this route would preserve the native structure and activity of these biochemical factors that otherwise would not

survive the steps involved in directly appending them to CNCs or coating the scaffolds with nanoparticles.

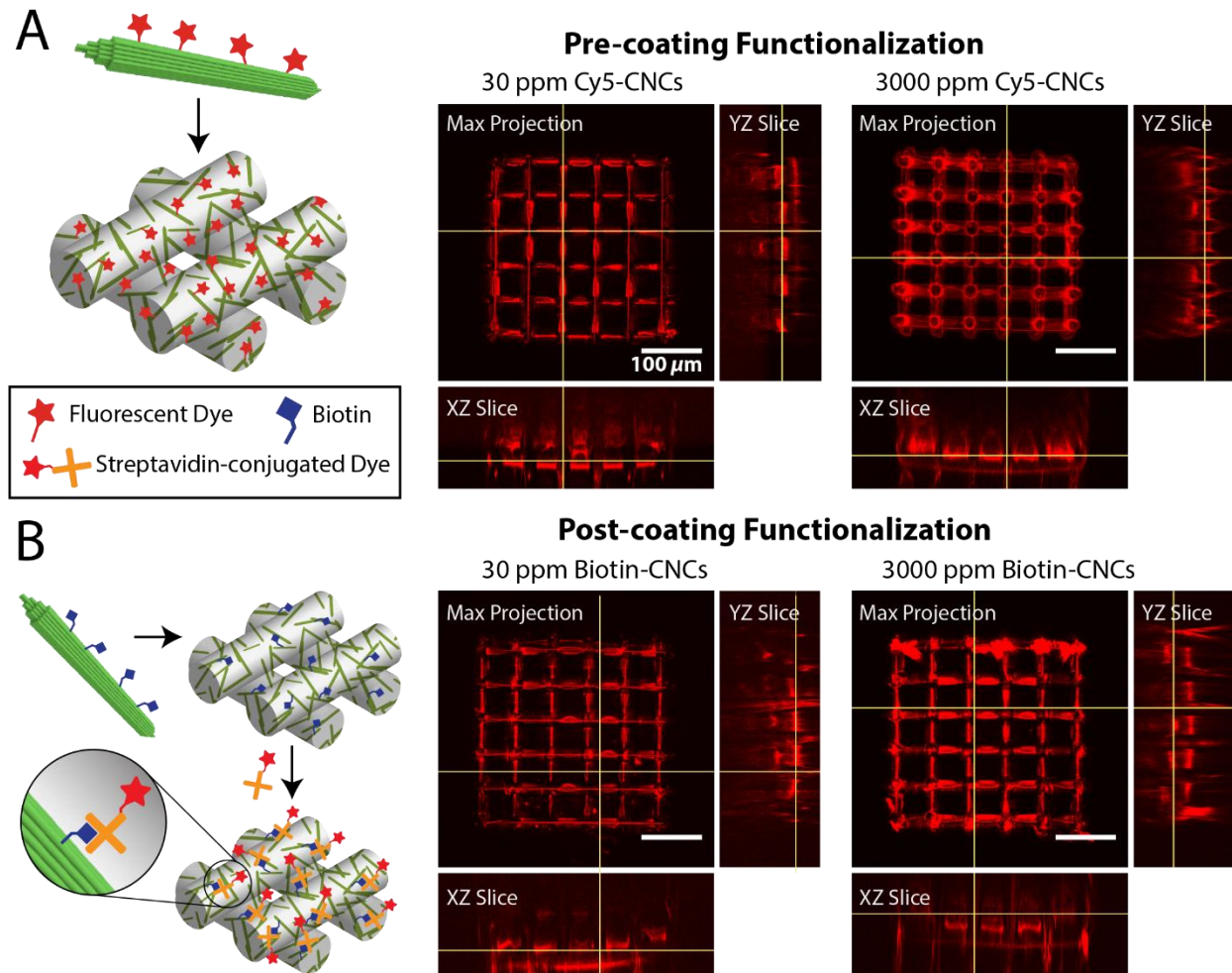


Figure 4: Coating and functionalization of 3D PEG-DA woodpiles with chemically-modified CNCs. The ability to functionalize 3D-printed PEG-DA structures with Cy5 was characterized using laser scanning confocal microscopy. Fluorescence z-stack images were acquired in the far-red channel with a slice thickness of 1.2 μm and a total depth of 180 μm . XY images were obtained using a maximum sum projection of the stack while YZ and XZ orthogonal projections were single slices taken at the positions indicated by the yellow lines.

The LbL dip-coating method has been previously used for the fabrication of multi-layered, nanostructured composite biomaterials that consist of CNCs, polyelectrolytes and other scaffolding polymers like collagen, chitosan and POEGMA.⁴¹⁻⁴³ While this method has been traditionally used for creating thin films or 2.5D structures, we have demonstrated that this approach can be extended to coat 3D-printed scaffolds with tuneable densities of CNCs. The ability to coat both DS3000 and PEG-DA, which possess contrasting physical and chemical properties, suggests that this method can be applied to other biomaterials commonly used in 3D-printing in order to confer nanotopography and functionalization. The versatility of this approach likely stems from the ability of PAH to non-specifically interact with various uncharged materials, as we observed that the introduction of surface negative charge through plasma treatment was not necessary to achieve coating. Despite the simplicity of this

method, some obstacles were encountered when coating 3D hydrogel scaffolds. Compared to DS3000, coating 3D-printed PEG-DA structures using this procedure was more challenging as the small hydrogels were delicate, exhibited high water retention and were easily detachable from the substrate. As a result, the numerous coating, washing and drying steps involved required careful handling of samples and avoidance of harsh drying methods such as the use of an air gun. As previously discussed, a key step to obtaining uniform and reproducible coatings was thoroughly washing away excess PAH, which would otherwise result in the formation of aggregate cellulose fibers and films. Achieving this required an intermediary drying step between washing, which we suspect is necessary for the PAH chains to collapse onto the PEG-DA scaffold in order to irreversibly coat it. This requirement may pose issues when coating more delicate scaffolds, where the process of dehydration could significantly deform or collapse fine structures.

2.4 Impact of CNC coatings on cellular attachment and morphology.

The impact of CNC coatings and their density on the adhesion and morphology of PC3-GFP prostate cancer cells was studied on PEG-DA and DS3000 3D-printed scaffolds. In the absence of CNCs, PC3 cells did not adhere to PEG-DA woodpiles (2 ± 2 bound cells/scaffold), as seen by spinning disk confocal microscopy (Figure 5). Coating the scaffold with CNCs using a 30 ppm solution caused some cells to bind to the PEG-DA hydrogel (35 ± 14 cells/scaffold) and a high coating concentration of 3000 ppm resulted in complete coverage of the woodpile with cells (97 ± 13 cells/scaffold). As seen in the fluorescence orthogonal projections and SEM micrographs, the cells were able to reside deep within the woodpile and occasionally suspended between beams when not lying flat or wrapping them. Staining with ethidium bromide homodimer did not result in red fluorescence from any of the cells, indicating that CNCs did not hinder cellular viability at both high and low coating concentrations after 2 days of cell culture. Unexpectedly, this dye was able to non-specifically stain CNCs and in this case highlighted the scaffold coating with a fluorescence intensity proportional to the density of CNCs.

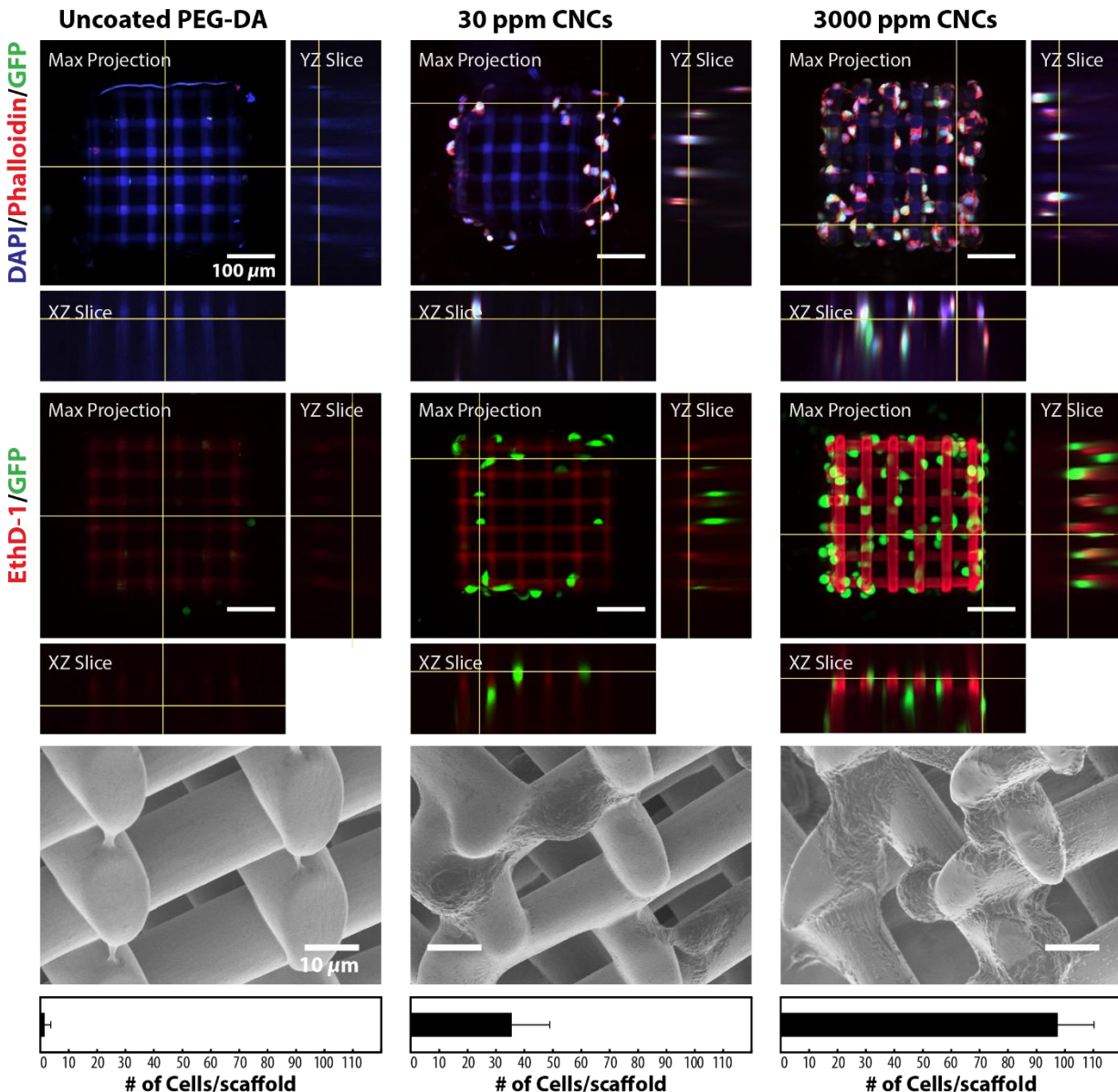


Figure 5. The adhesion of PC3-GFP prostate cancer cells to PEG-DA 3D woodpile structures could be tuned by the density of the CNC coatings. PC3-GFP prostate cancer cells, which constitutively expressed GFP, were seeded on the PEG-DA scaffolds at a density of $10,000 \text{ cells/cm}^2$ for one hour, supplemented with media, and cultured for 2 days. Images in the top row are of formalin-fixed cells stained for the nucleus and actin filaments using DAPI and Rhodamine-Phalloidin, respectively, and were acquired using spinning-disk confocal microscopy. The cells in the second row were cultured under the same conditions and stained with ethidium bromide homodimer (EthD-1), which causes dead cells to fluoresce in yellow (false-colored in red). The sample in the first row was dehydrated and imaged by SEM (bottom row). Cells were manually counted from the raw z-stack confocal images, and the bars at the bottom represent the average and standard deviation from at least 3 samples in each condition.

Coating PEG-DA with CNCs permitted attachment of the PC3 cells to the 3D scaffold in a fashion that was tuneable by controlling the surface density of CNCs. The ability of these nanoparticles to enhance the attachment of PC3 cells to PEG-DA, which was also observed with 2.5D structures (Supp. Figure 5), is not fully understood but we hypothesize that it arises from the presence of nanotopography, from the

increased hydrophobicity of the CNCs or from the higher local stiffness introduced by the rigid nanoparticles. The coverage of the hydrogel surface with CNCs may mask the protein-repelling properties of PEG-DA and in turn allow adhesion proteins, which are present on the cellular surface, to attach to the scaffold. This effect may be complemented by the chemical properties of the CNC surface, which presents both hydrophobic and hydrophilic facets that potentially pose as adhesion sites for the cells.^{44,45} Alternatively, the nanotopography and increase in surface roughness introduced by the CNCs, which have been previously shown to significantly enhance cellular adhesion, may provide more features for the cells to interact with and adhere to.^{46–48} The possibility of PAH being responsible for the enhanced cellular adhesion was ruled out with a control experiment on 2.5D PEG-DA structures coated only with PAH, where cells could not bind to the hydrogel (Supp. Figure 5). The concentration of PAH also remained constant when the woodpiles were coated with 30 ppm or 3000 ppm CNCs, while the observed cellular adhesion was concentration dependent on the CNC coating. Thus, it can be concluded that the enhanced adhesion was a direct result of the presence of CNCs.

Similar enhancements in cell binding were not observed for DS3000 scaffolds coated with CNCs (Figure 6). This material is designed to be bio-compatible and supported culturing of PC3 prostate cancer cells without any coatings. However, coating 2.5D DS3000 scaffolds with CNCs altered the morphology of PC3 cells. In uncoated scaffolds, PC3 cells appeared to organize in clusters and lay flat on the surface while adopting epithelial-like, polygon-shaped morphologies. Upon sparsely coating the scaffold with CNCs (30 ppm), the cells were more uniformly distributed along the scaffold and adopted elongated, multipolar configurations that are reminiscent of fibroblasts. When the scaffolds were densely coated with CNCs (3000 ppm), most of the cells were spherical and exhibited little to no cellular extensions. Similar trends in morphology were observed with PC3 cells cultured on 3D PEG-DA scaffolds densely coated with CNCs (Figure 5, Supp. Figure 5). However, it is difficult to make a comparison to pristine PEG-DA as little to no cells adhered. Given the propensity of PC3 cells to adhere to CNCs, as seen with coated PEG-DA, their morphology appeared to be dictated by the amount of CNCs present within their surroundings. With a moderate CNC density, the cells may have extended filopodia to sites where CNCs are present, hence giving rise to their elongated morphology. When the scaffold surface was completely covered with CNCs, the cells do not have tendency to extend to other areas as they are likely already in contact with CNCs. By tuning the density of CNCs present on the scaffold surface, it was possible to alter the morphology adopted by PC3 prostate cancer cells when cultured on DS300 and PEG-DA. In future work, this can be complemented with biochemical functionalization of the scaffolds to further recapitulate real cell microenvironments and guide the differentiation of cells to specific lineages. On the other hand, the control offered by CNC coatings on the adhesion of PC3 cells to PEG-DA scaffolds can be used for the development of medical devices that isolate rare circulating tumour cells from blood.

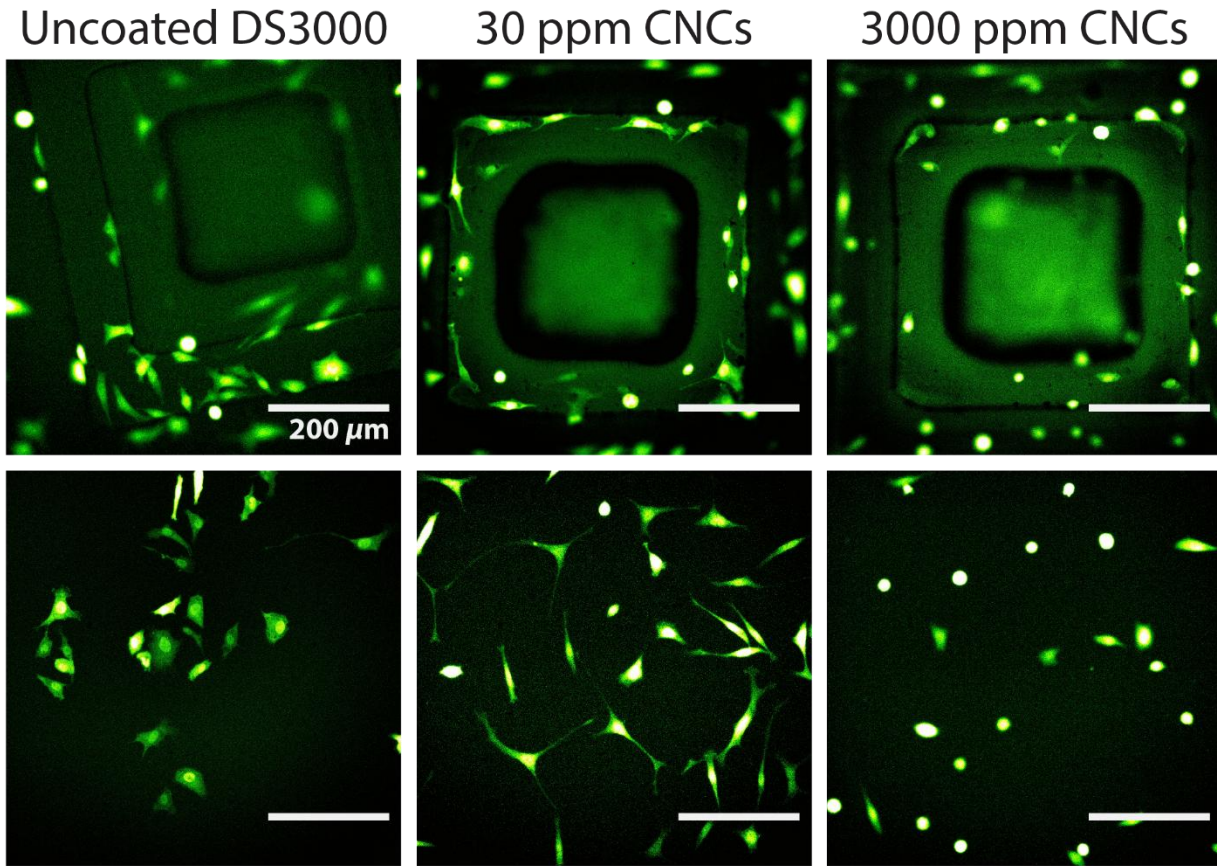


Figure 6. Epifluorescence images of PC3-GFP cells cultured on DS3000 2.5D pyramids. Cells were seeded at a density of 15,000 cells/cm² for one hour, supplemented with media, and cultured for 3 days. Live-cell images were acquired in the green channel using an epifluorescence microscope at room temperature. The top row consists of representative images of cells adhering to the pyramid while the images in the bottom row were acquired on the flat part of the DS3000 pyramid array.

3. CONCLUSION

The process of additive manufacturing through single- and two-photon polymerization 3D-printing systems allowed the fabrication of PEG-DA and DS3000 scaffolds with precise control on their size, hierarchy and geometric complexity. We have extended the method of layer-by-layer polyelectrolyte dip-coating with CNCs to introduce nanostructured topography and chemical functionalization onto the surface of 3D-printed structures in a tuneable and versatile fashion. Coating the scaffolds with various densities of CNCs enabled control on the adherence of GFP-PC3 prostate cancer cells to PEG-DA surfaces and altered the morphology of the cells when cultured on both PEG-DA and DS3000 structures. The mechanism by which CNCs influence the attachment and morphology of these cells remains unclear as it is challenging to decouple the effects of surface nanoroughness and surface chemistry that are simultaneously introduced by the CNCs. The versatility offered by biotin-CNCs in functionalizing scaffolds with streptavidin-conjugated molecules allows future explorations on using biochemical factors to further mimic real cellular microenvironments. Fabricating realistic cellular scaffolds would promote the desirable cellular behaviour that is necessary to study fundamental biological concepts and creating artificial tissue, organoid models and medical devices.

Acknowledgments

This work was supported by the French RENATECH network. It was partly supported as part of the MultiFAB project funded by FEDER European Regional Funds and French Région Occitanie (grant agreement number 16007407/MP0011594) and by the HoliFAB project funded by the European Union's Horizon 2020 research and innovation program (grant agreement No 760927).

4. EXPERIMENTAL SECTION

4.1 Materials.

3-(Trimethoxysilyl)propyl methacrylate (98% , TPM), poly(ethylene glycol) diacrylate (PEG-DA, Mn = 700 Da, n = 1.47), diphenyl(2,4,6-trimethylbenzoyl)phosphine oxide (Irgacure® 819), Triton X-100, 10% formalin and 99% acetic acid were purchased from Sigma-Aldrich (**City, State, Country**). DS3000 negative tone resist was purchased from DWS Systems (Italy). Poly(allylamine hydrochloride) (PAH, Mw = 120,000 – 200,000 Da) was purchased from Polysciences (Warrington, PA, USA) and stored at -20 °C. Cellulose nanocrystals (CNCs, spray-dried), were kindly donated by CelluForce Inc. (Montreal, QC, Canada) and were previously characterized by dynamic light scattering, atomic force microscopy and X-ray diffraction to have an average hydrodynamic radius of 70 ± 3 nm, zeta potential of -39 ± 1 mV, length of 183 ± 88 nm, cross-section of 6 ± 2 , and crystallinity of 90%, respectively.⁴⁹ All mentions of water refer to double-distilled 18.2 MΩ water (ddH₂O, ultrapure, type I), generated from a Milli-Q Direct purifier system (Millipore Sigma). Cy5-conjugated streptavidin (0.1 mg/mL in PBS with 4 mg/mL BSA) was purchased from ThermoFisher Scientific (**City, State, Country**).

4.2 Functionalization of CNCs with Cy5 and biotin.

CNCs were functionalized with Cy5 or biotin using triazine click-chemistry as described in previous work.^{32,50} Since trichlorotriazine presents a site of substitution at each chlorine, grafting this molecule onto the CNC surface hydroxyl groups allows it to be used as a linker when other sites are reacted with the functionality of interest. A more general implementation of this involved appending, to the triazine linker, a group that can participate in a click-reaction with a molecule of interest that presents a complementary chemical handle. Many widely used functionalities, such as dyes and ligands, are commercially available with chemical handles that are compatible for click-reactions. To this end, CNCs were grafted with: i) dichlorotriazine-alkyne, to which azido-Cy5 was conjugated, or ii) dichlorotriazine-PEG₇₋₈-azide, to which alkyne-biotin was conjugated (**make Supp. Figure of these reaction schemes**).

4.3 Silanization of glass coverslips and ITO-coated slides.

Glass substrates were silanized with a methacrylate group to ensure proper adhesion of spin-coated thin films. Circular glass coverslips (No. 1.5, 18 mm diameter, 170 µm nominal thickness, VWR, **City, state, country**) or indium-tin-oxide (ITO)-coated glass slides (25 x 25 mm, 0.7 mm thickness,

Nanoscribe GMBH, Karlsruhe, Germany) were sequentially cleaned with acetone, ethanol and water then dried with an air gun. The glass or ITO surface was activated with a Diener Electronic air plasma machine (5 mins, 0.6 mbar, 30 W) immediately before drop-casting TPM (2% v/v in ddH₂O with 0.1% v/v of acetic acid) over the substrates. The droplets of the TPM solution were kept for 2 hrs before rinsing the substrates with ethanol and ddH₂O then drying with an air gun.

4.4 Spin-coating thin films of PEG-DA and DS3000 on circular glass substrates.

DS3000 was spin-coated onto silanized 18 mm glass slides (5000 rpm, 60 s, 1000 rpm/s) using a Suss MicroTec spin-coater (Karl Suss, Garching, Germany) and cured immediately with a flood exposure of 405 nm light (60 s, 30 mW/cm²) using a Suss MicroTec MA/BA6 mask aligner (Karl Suss, Garching, Germany). The samples were rinsed in ethanol for 10 s then dried with an air gun. PEG-DA thin-films were prepared the same way but on DS3000-coated glass coverslips to improve adhesion.

4.5 3D-printing DS3000 using single-photon polymerization.

DS3000 structures were fabricated using a laser-assisted stereolithography; DWS 029J+ 3D-printer from DWS Systems. The system was equipped with a 405 nm laser (86 mW, Solid State BluEdge BE-1800C) and a galvanometric mirror that can achieve a maximum scanning speed of 6000 mm/s. In order for the samples to adhere to the substrate, the first four layers were overisolated by reducing the scanning speed to 200 mm/s, whereas the rest of the structure was printed at 3000 mm/s. The hatching and slicing distances were set to 40 μm and 50 μm, respectively. The 2.5D pyramids, which consisted of three, 50 μm-high steps with side lengths of 700, 500 and 300 μm, were printed as an array on a circular base with a diameter of 20 mm and 2 mm thickness. The 3D bone scaffold was printed similarly to previous works [ref].

4.6 3D-printing PEG-DA using two-photon polymerization direct laser writing.

PEG-DA structures were 3D-printed by two-photon polymerization (2PP) direct laser writing using Nanoscribe Photonics Professional GT2 (Karlsruhe, Germany) system similar to previous work.^{37,46,51–53} Briefly, PEG-DA 700 was thawed (from -20 °C) for an hour at r.t., combined with photoinitiator Irgacure 819 to a concentration of 0.5% w/w and stirred for 3 hrs in the dark. Water was added to make a 3:1 PEG-DA:water solution and stirred overnight at r.t. in the dark. Silanized ITO glass slides were coated with DS3000, using the same procedure as above, to improve the adhesion of PEG-DA to the substrate and allow the microscope to find the substrate interface. The substrate was fixed onto a dip-in laser lithography (DiLL) holder and a droplet of the PEG-DA solution was placed in the center. The holder was inverted and mounted onto the stage of the Nanoscribe. In such configuration, the employed 2PP objective is directly immersed in the photosensitive liquid. The 2PP setup system consisted of an inverted two-photon Carl Zeiss microscope, coupled to a 780 nm femtosecond pulsed fiber laser (100 fs, 50 mW, FemtoFiber Pro, Toptica Photonics), with a resonating scanner and a galvanometric mirrors system allowing a moving-beam fixed-sample configuration. The sample was approached with a 25x (NA 0.8) water-immersion objective, with the collar set a quarter way from the glycerol mark to the water mark, until the lens was in immersion with the resin and the interface between the substrate and the photosensitive PEG-DA interface was found. The structures of interest were designed beforehand using CAD software Autodesk Fusion 360 and imported as a work file into Nanoscribe with both the hatching and slicing distance writing parameters equal to 400 nm. The 2.5D pillar array design, which consisted of a 300 x 300 x 15 μm base, half-covered with 5 μm diameter pillars, 10 μm apart, was printed with a writing speed of 25 mm/s and a nominal laser power of 70%. The 3D woodpile design (270 x 270 x 280

μm) consisted of perpendicularly stacked layers, each composed of 20 μm diameter cylinders interspaced 50 μm apart. This structure was printed four times on each sample with different laser powers of 76%, 78%, 79% and 80% and a writing speed of 50 mm/s.

4.7 Dip-coating thin-films and 3D-printed structures with CNCs.

Spray-dried CNCs were dissolved in ddH₂O to make a 3 wt% (30,000 ppm) suspension through repeated cycles of vortex mixing and dispersion with a VC334 Vibracell point probe sonicator (100 W, 2 s pulses, 6 min with 3 mm tapered microtip) until it was clear. Through serial dilutions of this solution, 3000 - 3 ppm CNC suspensions were prepared and dispersed with point probe sonication after each dilution. To dip-coat structures with CNCs, it was first necessary to coat them with PAH, which was prepared from powder form to make a 1 wt% solution. The PAH solution was used within two weeks, while all the CNC solutions with a concentration lower than 3000 ppm were prepared fresh each time as they could be significantly depleted with each coating.

To ensure adequate wettability, 3D-printed DS300 structures were first activated with air plasma (3 mins, 0.6 mbar, 30 W). 3D-printed PEG-DA structures were not plasma activated as they were stored in water after printing to avoid collapse of the hydrogel. The samples were then “dipped”, or placed, into a plastic petri dish containing 20 mL of PAH for 15 mins. To wash off excess PAH, the samples were placed in a ddH₂O dish for 10 mins, air dried then placed in another ddH₂O dish for 10 mins. The structures were then dipped into a 20 mL solution of CNCs for 15 mins, washed in a ddH₂O dish for 10 mins and air-dried. Thin films and 3D-printed DS3000 samples could be dried using an air gun, while PEG-DA structures were left to slowly dry at r.t. as they could easily detach from the substrate in the presence of strong airflow.

4.8 Functionalization of 3D scaffolds.

3D structures were coated using the dip-coating method with a layer of CNCs, 10% of which were functionalized with either Cy5 or biotin. For post-coating functionalization, the PEG-DA woodpile scaffold was incubated with 100 μL 0.01 mg/mL of Cy5-streptavidin in PBS for 30 mins within a Pyrex cloning cylinder then washed for 30 mins in PBS.

4.9 Culture of PC3-GFP prostate cancer cells.

A 1.5 cm x 1.5 cm frame cut from double-sided adhesive tape (0.25 mm thick, ThermoFisher) was placed on the center of a glass substrate including the 3D-printed PEG-DA structures. The samples were sterilized with 70% ethanol for 30 mins, rinsed with PBS and PC3-GFP cells were seeded within the frame (to confine the seeding area and minimize the number of cells used during the inoculation step) at a density of 10,000 cells/cm² and incubated for one hour (37°C, 5% CO₂). The cells were supplemented with media (DMEM with 10% SVF, 1% penicillin/streptomycin and 1% geneticin) and cultured for 1 or 2 days on the 2.5D or 3D structures, respectively. DS3000 2.5D structures were cultured with PC3-GFP cells in a similar fashion, but an additional washing step of 2 days in PBS was done before dip-coating and cell culture. The structures, without a frame, were placed in a 6-well cell culture plate, seeded with 15,000 cells/cm² and cultured for 3 days.

Cells cultured on 2.5D DS3000 or PEG-DA structures (Figure 6, Supp. Figure 5) were imaged live, without staining or fixation. Cells cultured on 3D PEG-DA woodpile structures (Figure 5a) were fixed with 10% formalin for 30 mins, permeabilized with 0.2% Triton X-100 for 3 mins and stained for actin and nuclear DNA with Rhodamine-Phalloidin (Invitrogen, 16.5 mg/mL, 30 mins, r.t.) and DAPI (Invitrogen, 10

$\mu\text{g/mL}$, 15 mins, r.t.), respectively. This sample was then dehydrated with consecutive ethanol baths (50%, 70%, 90% and 100% for 4 mins/bath) and air dried before being imaged with SEM (Figure 5c). To test for the presence of dead cells, duplicate samples were red stained with 4 μM ethidium bromide homodimer (live/dead kit for mammalian cells, Invitrogen) for 30 mins at 37°C. Cell counting was done manually using the multi-point tool in ImageJ.

4.10 Characterization of surface roughness and CNC coating density with AFM.

The nanostructure and roughness arising from the CNC coating process and its response to variations in CNC concentrations was assessed using a Bruker ICON AFM. All images were acquired in tapping mode with a Bruker FESP cantilever of a spring constant of 1 – 5 N/m and a resonating frequency of 72 kHz. Areas of 2.5 $\mu\text{m} \times 2.5 \mu\text{m}$ were scanned at 3 or more random locations on each thin film, the flat side of the PEG-DA 2.5D pillar arrays or the top of the DS3000 pyramids, with 256 lines at a rate of 0.5 lines/s. Image correction, including plane levelling and row alignment, and analysis were performed with Gwydion 2.47. RMS roughness, S_q , was calculated by this software using the following formula, where z_n and \bar{z} represent the height and mean height, respectively:

$$S_q = \sqrt{\frac{1}{N} \sum_{n=1}^N (z_n - \bar{z})^2}$$

4.11 Laser scanning confocal microscopy imaging of scaffolds coated with functionalized CNCs.

The functionalization of 3D-printed structures with Cy5 was characterized in terms of coverage and density using a Leica SP8 DM6000CS laser scanning confocal microscope. All samples were excited with a 638 nm, 30 mW, diode laser (LASOS, Jena, Germany) and fluorescence was collected by a spectral photomultiplier tube detector (type?) set to an emission band of 730 – 800 nm. Images of PEG-DA woodpile structures were acquired using the LAS X software with a 20 \times /NA0.7 water immersion objective using xy- and z-steps of 0.45 and 1.2 μm , respectively. Laser power compensation, where higher laser intensities were used at deeper sections, was employed in an attempt to completely visualize the structure. DS3000 bone scaffolds were imaged similarly, however, given their centimeter sizes, it was not possible to image them in their entirety. To this end, images of control and coated samples were all acquired using the same conditions, where 1.5 x 1.5 x 0.75 mm sections were captured using a 10 \times /NA0.3 air objective, 10% laser power and xyz-steps of 3 μm . Orthogonal projections and 3D renders were produced with ImageJ software.

4.12 Spinning disk confocal imaging of PC3 cancer cells on PEG-DA 3D woodpiles.

Cells cultured on 3D scaffolds were imaged using a Leica DMI8 inverted microscope controlled with imaging software ImageJ MicroManager and equipped with a Yokogawa CSU-X1 spinning disk confocal, 405 nm and 488 nm diode, 100 mW lasers and a 561 nm, diode-pumped solid state, 100 mW laser. Emitted light was collected with a 50 μm Nipkow disk spinning at 5,000 rpm before being filtered by a 450/50 nm, 525/50 nm or 595/50 nm bandpass filter and captured by a Flash 4.0 v3 Hamamatsu camera. The samples were inverted and mounted onto a No 1.5 glass coverslip with a 0.25 mm thick double-sided sticky frame to create an aqueous chamber of cell medium and allow imaging with the inverted microscope. Images were captured using a 10 \times /NA0.45 water immersion objective using an exposure of 200 ms and 2 μm z-steps.

4.13 Epifluorescence imaging of PC3s on 2.5D DS3000 and PEG-DA structures.

PC3-GFP cells were imaged with an Olympus BX51 upright epifluorescence microscope using a 10×NA0.3 objective and an X-Cite 120 lamp. Emitted light was filtered through a 545/55 nm bandpass filter and captured by a Hamamatsu C13440 ORCA-Flash4.0 CMOS digital camera controlled by imaging software ImageJ MicroManager.

4.14 SEM characterization of 3D-printed structures.

3D-printed samples were imaged with an Hitachi S-4800 system set to a working accelerating voltage and current of 0.7 kV and 10 µA, respectively, at a distance of 12.8 mm. Secondary electrons were detected by an _____ detector.

5. REFERENCES

1. Inzana, J. A. *et al.* 3D printing of composite calcium phosphate and collagen scaffolds for bone regeneration. *Biomaterials* **35**, 4026–4034 (2014).
2. Hockaday, L. A. *et al.* Rapid 3D printing of anatomically accurate and mechanically heterogeneous aortic valve hydrogel scaffolds. *Biofabrication* **4**, 035005 (2012).
3. Li, K., Wang, D., Zhao, K., Song, K. & Liang, J. Electrohydrodynamic jet 3D printing of PCL/PVP composite scaffold for cell culture. *Talanta* **211**, 120750 (2020).
4. Kim, D. H., Provenzano, P. P., Smith, C. L. & Levchenko, A. Matrix nanotopography as a regulator of cell function. *Journal of Cell Biology* vol. 197 351–360 (2012).
5. Krishna, L. *et al.* Nanostructured scaffold as a determinant of stem cell fate. *Stem Cell Research and Therapy* vol. 7 1–12 (2016).
6. Yim, E. K. F. & Leong, K. W. Significance of synthetic nanostructures in dictating cellular response. *Nanomedicine: Nanotechnology, Biology, and Medicine* vol. 1 10–21 (2005).
7. Canty, E. G. *et al.* Coalignment of plasma membrane channels and protrusions (fibropositors) specifies the parallelism of tendon. *Journal of Cell Biology* **165**, 553–563 (2004).
8. Baselt, D. R., Revel, J. P. & Baldeschwieler, J. D. Subfibrillar structure of type I collagen observed by atomic force microscopy. *Biophysical journal* **65**, 2644–55 (1993).
9. Provenzano, P. P. & Keely, P. J. Mechanical signaling through the cytoskeleton regulates cell proliferation by coordinated focal adhesion and Rho GTPase signaling. *Journal of Cell Science* **124**, 1195–1205 (2011).
10. Dickinson, R. B., Guido, S. & Tranquillo, R. T. Biased cell migration of fibroblasts exhibiting contact guidance in oriented collagen gels. *Annals of Biomedical Engineering* **22**, 342–356 (1994).
11. Provenzano, P. P., Inman, D. R., Eliceiri, K. W., Trier, S. M. & Keely, P. J. Contact guidance mediated three-dimensional cell migration is regulated by Rho/ROCK-dependent matrix reorganization. *Biophysical Journal* **95**, 5374–5384 (2008).

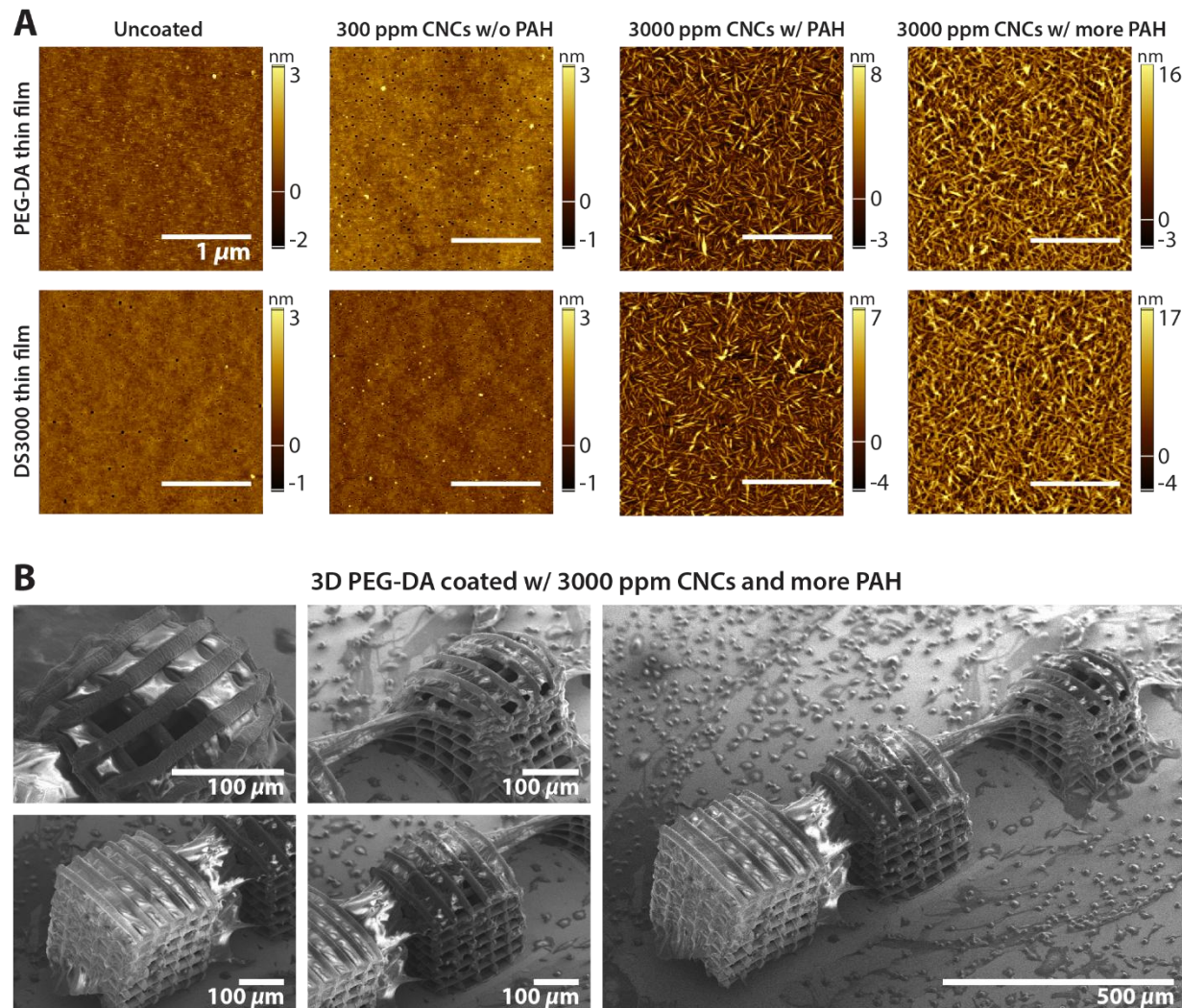
12. Wang, W. *et al.* Single Cell Behavior in Metastatic Primary Mammary Tumors Correlated with Gene Expression Patterns Revealed by Molecular Profiling. *Cancer Research* **62**, (2002).
13. Abrams, G. A., Goodman, S. L., Nealey, P. F., Franco, M. & Murphy, C. J. Nanoscale topography of the basement membrane underlying the corneal epithelium of the rhesus macaque. *Cell and Tissue Research* **299**, 39–46 (2000).
14. Liliensiek, S. J., Nealey, P. & Murphy, C. J. Characterization of endothelial basement membrane nanotopography in rhesus macaque as a guide for vessel tissue engineering. *Tissue engineering. Part A* **15**, 2643–2651 (2009).
15. Karuri, N. W. *et al.* Biological length scale topography enhances cell-substratum adhesion of human corneal epithelial cells. *Journal of Cell Science* **117**, 3153–3164 (2004).
16. Dalby, M. J., Riehle, M. O., Sutherland, D. S., Agheli, H. & Curtis, A. S. G. Changes in fibroblast morphology in response to nano-columns produced by colloidal lithography. *Biomaterials* **25**, 5415–5422 (2004).
17. Lee, M. R. *et al.* Direct differentiation of human embryonic stem cells into selective neurons on nanoscale ridge/groove pattern arrays. *Biomaterials* **31**, 4360–4366 (2010).
18. Teixeira, A. I., Abrams, G. A., Bertics, P. J., Murphy, C. J. & Nealey, P. F. Epithelial contact guidance on well-defined micro- and nanostructured substrates. *Journal of Cell Science* **116**, 1881–1892 (2003).
19. Dalby, M. J. *et al.* Attempted endocytosis of nano-environment produced by colloidal lithography by human fibroblasts. *Experimental Cell Research* **295**, 387–394 (2004).
20. Lee, C. H. *et al.* Nanofiber alignment and direction of mechanical strain affect the ECM production of human ACL fibroblast. *Biomaterials* **26**, 1261–1270 (2005).
21. Makaremi, S. *et al.* The Topography of Silica Films Modulates Primary Macrophage Morphology and Function. *Advanced Materials Interfaces* **6**, 1900677 (2019).
22. Melchels, F. P. W., Feijen, J. & Grijpma, D. W. A review on stereolithography and its applications in biomedical engineering. *Biomaterials* vol. 31 6121–6130 (2010).
23. Guillaume, O. *et al.* Surface-enrichment with hydroxyapatite nanoparticles in stereolithography-fabricated composite polymer scaffolds promotes bone repair. *Acta Biomaterialia* **54**, 386–398 (2017).
24. Tang, Y., Zhao, Y., Wang, X. & Lin, T. Layer-by-layer assembly of silica nanoparticles on 3D fibrous scaffolds: Enhancement of osteoblast cell adhesion, proliferation, and differentiation. *Journal of Biomedical Materials Research Part A* **102**, 3803–3812 (2014).
25. Lee, J. H., Lee, J. Y., Yang, S. H., Lee, E. J. & Kim, H. W. Carbon nanotube-collagen three-dimensional culture of mesenchymal stem cells promotes expression of neural phenotypes and secretion of neurotrophic factors. *Acta Biomaterialia* **10**, 4425–4436 (2014).
26. Hirata, E. *et al.* Multiwalled carbon nanotube-coating of 3D collagen scaffolds for bone tissue engineering. *Carbon* **49**, 3284–3291 (2011).

27. Jung, Y. *et al.* In situ chondrogenic differentiation of human adipose tissue-derived stem cells in a TGF- β 1 loaded fibrin-poly(lactide-caprolactone) nanoparticulate complex. *Biomaterials* **30**, 4657–4664 (2009).
28. Engler, A. J., Sen, S., Sweeney, H. L. & Discher, D. E. Matrix Elasticity Directs Stem Cell Lineage Specification. *Cell* **126**, 677–689 (2006).
29. Moon, R. J., Martini, A., Nairn, J., Simonsen, J. & Youngblood, J. Cellulose nanomaterials review: Structure, properties and nanocomposites. *Chemical Society Reviews* vol. 40 3941–3994 (2011).
30. Habibi, Y., Lucia, L. A. & Rojas, O. J. Cellulose nanocrystals: Chemistry, self-assembly, and applications. *Chemical Reviews* **110**, 3479–3500 (2010).
31. Gill, U. *et al.* Beyond buckling: Humidity-independent measurement of the mechanical properties of green nanobiocomposite films. *Nanoscale* **9**, 7781–7790 (2017).
32. Fatona, A., Berry, R. M., Brook, M. A. & Moran-Mirabal, J. M. Versatile Surface Modification of Cellulose Fibers and Cellulose Nanocrystals through Modular Triazinyl Chemistry. *Chemistry of Materials* **30**, 2424–2435 (2018).
33. Hu, H. *et al.* Redox-Responsive Polycation-Functionalized Cotton Cellulose Nanocrystals for Effective Cancer Treatment. *ACS Applied Materials and Interfaces* **7**, 8942–8951 (2015).
34. Despres, H. W. *et al.* Mechanisms of the immune response cause by cationic and anionic surface functionalized cellulose nanocrystals using cell-based assays. *Toxicology in Vitro* **55**, 124–133 (2019).
35. Wan, W. *et al.* Direct Surface Functionalization of Cellulose Nanocrystals with Hyperbranched Polymers through the Anionic Polymerization for pH-Responsive Intracellular Drug Delivery. (2019) doi:10.1021/acssuschemeng.9b05231.
36. Domingues, R. M. A., Gomes, M. E. & Reis, R. L. The potential of cellulose nanocrystals in tissue engineering strategies. *Biomacromolecules* vol. 15 2327–2346 (2014).
37. de France, K. J. *et al.* Tissue Response and Biodistribution of Injectable Cellulose Nanocrystal Composite Hydrogels. *ACS Biomaterials Science and Engineering* **5**, 2235–2246 (2019).
38. Moreau, C., Beury, N., Delorme, N. & Cathala, B. Tuning the architecture of cellulose nanocrystal-poly(allylamine hydrochloride) multilayered thin films: Influence of dipping parameters. *Langmuir* **28**, 10425–10436 (2012).
39. Martin, C. & Jean, B. Nanocellulose/polymer multilayered thin films: Tunable architectures towards tailored physical properties. *Nordic Pulp and Paper Research Journal* **29**, 19–30 (2014).
40. Liu, X., Holzwarth, J. M. & Ma, P. X. Functionalized Synthetic Biodegradable Polymer Scaffolds for Tissue Engineering. *Macromolecular Bioscience* **12**, 911–919 (2012).
41. Mesquita, J. P. de *et al.* Hybrid layer-by-layer assembly based on animal and vegetable structural materials: multilayered films of collagen and cellulose nanowhiskers. *Soft Matter* **7**, 4405–4413 (2011).

42. Huang, C. *et al.* Bio-inspired nanocomposite by layer-by-layer coating of chitosan/hyaluronic acid multilayers on a hard nanocellulose-hydroxyapatite matrix. *Carbohydrate Polymers* **222**, 115036 (2019).
43. de France, K. J. *et al.* 2.5D Hierarchical Structuring of Nanocomposite Hydrogel Films Containing Cellulose Nanocrystals. *ACS Applied Materials and Interfaces* **11**, 41 (2019).
44. Biermann, O. *et al.* Hydrophilicity and Lipophilicity of Cellulose Crystal Surfaces. *Angew. Chem. Int. Ed* **40**, (2001).
45. Mazeau, K. On the external morphology of native cellulose microfibrils. *Carbohydrate Polymers* **84**, 524–532 (2011).
46. Or, T. *et al.* Patterned cellulose nanocrystal aerogel films with tunable dimensions and morphologies as ultra-porous scaffolds for cell culture. *ACS Applied Nano Materials* **2**, 4169–4179 (2019).
47. Mo, Y. *et al.* Preparation and properties of PLGA nanofiber membranes reinforced with cellulose nanocrystals. *Colloids and Surfaces B: Biointerfaces* **132**, 177–184 (2015).
48. Sa Liu *et al.* High internal phase emulsions stabilised by supramolecular cellulose nanocrystals and their application as cell-adhesive macroporous hydrogel monoliths. *Journal of Materials Chemistry B* **5**, 2671–2678 (2017).
49. Reid, M. S., Villalobos, M. & Cranston, E. D. Benchmarking Cellulose Nanocrystals: From the Laboratory to Industrial Production. *Langmuir* **33**, 1583–1598 (2016).
50. de France, K. J. *et al.* Tissue Response and Biodistribution of Injectable Cellulose Nanocrystal Composite Hydrogels. *ACS Biomaterials Science and Engineering* **5**, 2235–2246 (2019).
51. Ferreira, F. v. *et al.* Porous nanocellulose gels and foams: Breakthrough status in the development of scaffolds for tissue engineering. *Materials Today* (2020) doi:10.1016/j.mattod.2020.03.003.
52. de France, K. J. *et al.* 2.5D Hierarchical Structuring of Nanocomposite Hydrogel Films Containing Cellulose Nanocrystals. *ACS Applied Materials and Interfaces* (2019) doi:10.1021/acsami.8b16232.
53. Riesco, R. *et al.* Water-in-PDMS Emulsion Templating of Highly Interconnected Porous Architectures for 3D Cell Culture. *ACS Applied Materials and Interfaces* (2019) doi:10.1021/acsami.9b07564.
54. Kilian, K. A., Bugarija, B., Lahn, B. T. & Mrksich, M. Geometric cues for directing the differentiation of mesenchymal stem cells. *Proceedings of the National Academy of Sciences of the United States of America* **107**, 4872–4877 (2010).
55. Krishna, L. *et al.* Nanostructured scaffold as a determinant of stem cell fate. *Stem Cell Research and Therapy* vol. 7 (2016).
56. Huang, D. M. *et al.* The promotion of human mesenchymal stem cell proliferation by superparamagnetic iron oxide nanoparticles. *Biomaterials* **30**, 3645–3651 (2009).

57. Huang, D. M. *et al.* Internalization of mesoporous silica nanoparticles induces transient but not sufficient osteogenic signals in human mesenchymal stem cells. *Toxicology and Applied Pharmacology* **231**, 208–215 (2008).
58. Kim, K. J. *et al.* Silica nanoparticles increase human adipose tissue-derived stem cell proliferation through ERK 1/2 activation. *International Journal of Nanomedicine* **10**, 2261–2272 (2015).
59. Tran, D. N., Ota, L. C., Jacobson, J. D., Patton, W. C. & Chan, P. J. Influence of nanoparticles on morphological differentiation of mouse embryonic stem cells. *Fertility and Sterility* **87**, 965–970 (2007).
60. Chao, T. I. *et al.* Carbon nanotubes promote neuron differentiation from human embryonic stem cells. *Biochemical and Biophysical Research Communications* **384**, 426–430 (2009).
61. Gou, X. *et al.* Mechanical property of PEG hydrogel and the 3D red blood cell microstructures fabricated by two-photon polymerization. *Applied Surface Science* **416**, 273–280 (2017).
62. Hirata, E. *et al.* Development of a 3D collagen scaffold coated with multiwalled carbon nanotubes. *Journal of Biomedical Materials Research Part B: Applied Biomaterials* **90B**, 629–634 (2009).
63. AOKI, N., AKASAKA, T., WATARI, F. & YOKOYAMA, A. Carbon Nanotubes as Scaffolds for Cell Culture and Effect on Cellular Functions. *Dental Materials Journal* **26**, 178–185 (2007).
64. Shrestha, B. K. *et al.* Bio-inspired hybrid scaffold of zinc oxide-functionalized multi-wall carbon nanotubes reinforced polyurethane nanofibers for bone tissue engineering. *Materials and Design* **133**, 69–81 (2017).
65. Sun, H. *et al.* Carbon nanotube-incorporated collagen hydrogels improve cell alignment and the performance of cardiac constructs. *International Journal of Nanomedicine* **12**, 3109–3120 (2017).
66. Cho, Y. & Borgens, R. ben. The effect of an electrically conductive carbon nanotube/collagen composite on neurite outgrowth of PC12 cells. *Journal of Biomedical Materials Research Part A* **95A**, 510–517 (2010).
67. Lee, J. H. *et al.* Combined effects of porous hydroxyapatite and demineralized bone matrix on bone induction: in vitro and in vivo study using a nude rat model. *Biomedical Materials* **6**, 015008 (2011).
68. Harunaga, J. S. & Yamada, K. M. Cell-matrix adhesions in 3D. *Matrix Biology* vol. 30 363–368 (2011).
69. Accardo, A. *et al.* Two-photon lithography and microscopy of 3D hydrogel scaffolds for neuronal cell growth. *Biomedical Physics and Engineering Express* (2018) doi:10.1088/2057-1976/aaab93.

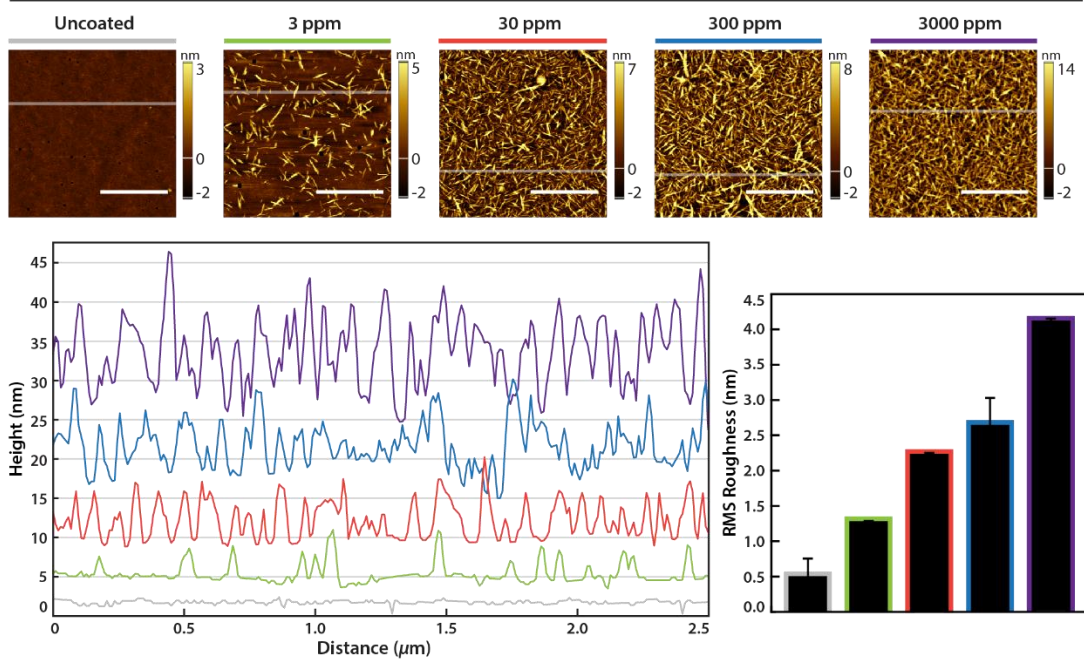
6. SUPPORTING INFORMATION



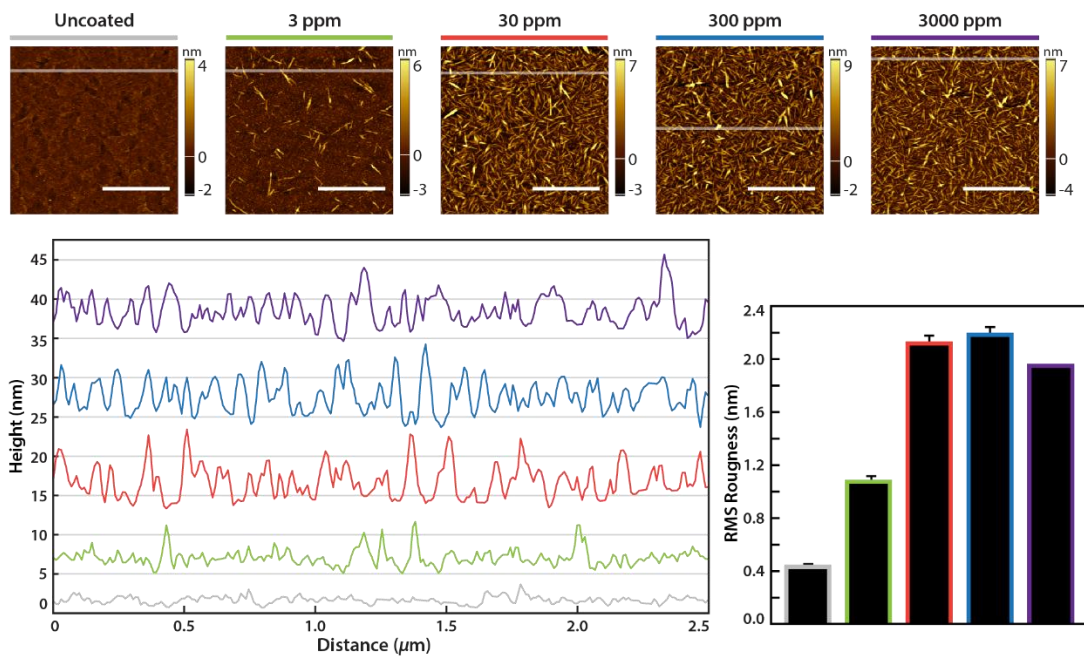
Supplementary Figure 1. The important role of PAH and its complete washing in coating thin films and 3D structures with CNCs. **A)** PEG-DA and DS3000 thin films were either uncoated or coated with 300 ppm CNCs without using PAH, or with 3000 ppm CNCs using PAH that was either washed with one (incomplete) or two (complete) steps. Without PAH, no CNCs adsorb onto the surface of the thin films, while excess PAH due to incomplete washing causes fibrillation of the CNCs. **B)** 3D PEG-DA woodpile structures coated with 3000 ppm CNCs without complete washing of PAH resulted in clogging, webbing and bridging of the structures. Culturing of PC3-GFP prostate cancer resulted in complete coverage of the structures with cells and occasionally cells were suspended within the cellulose films that bridged different structures.

A

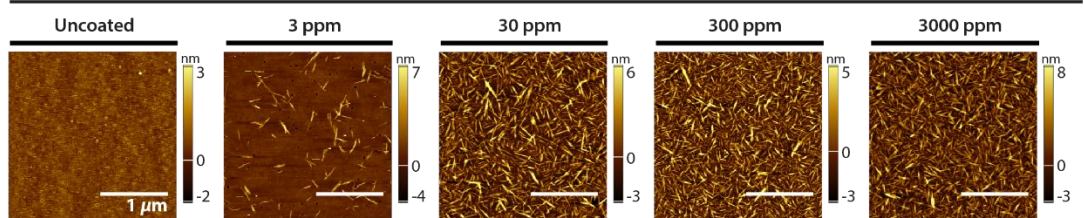
DS3000 thin film coated with incomplete washing of PAH

**B**

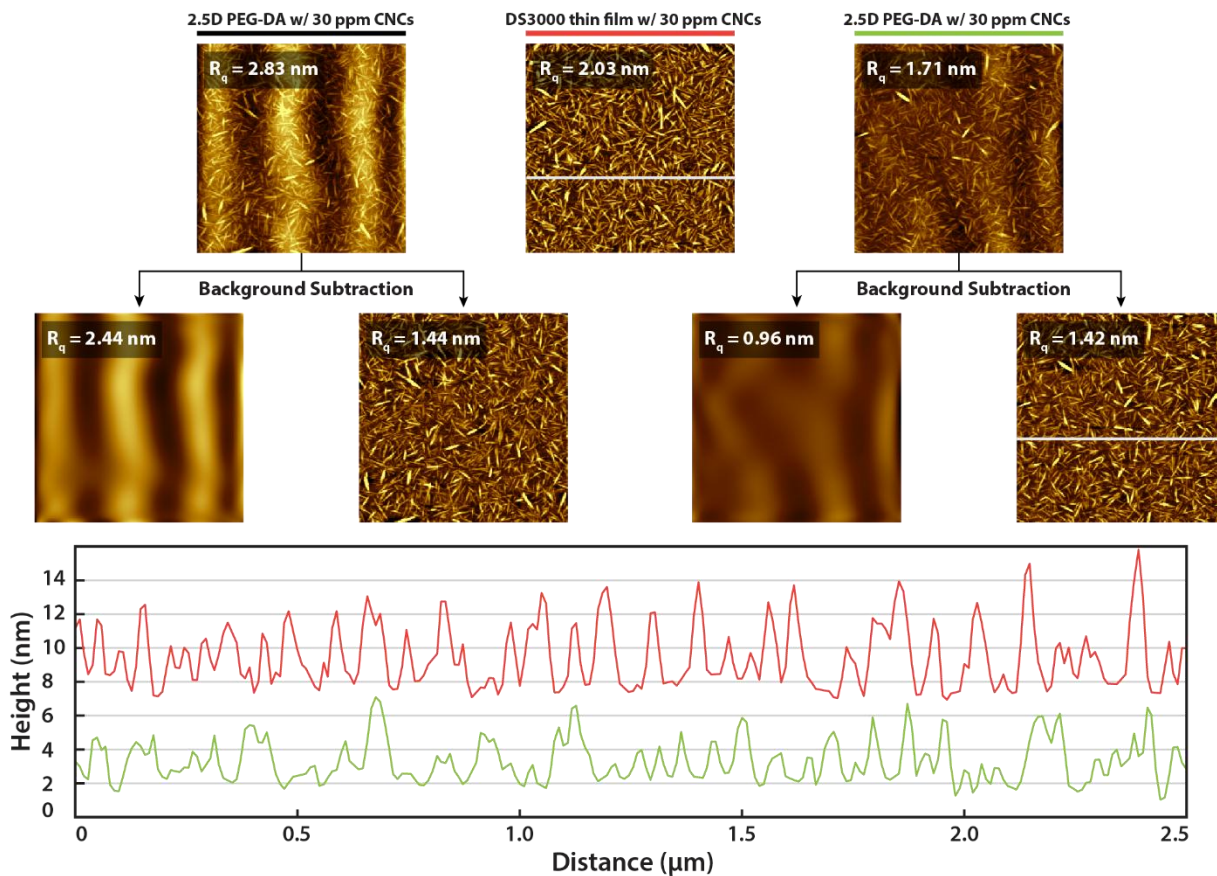
DS3000 thin film coated with complete washing of PAH

**C**

PEG-DA thin film coated with complete washing of PAH

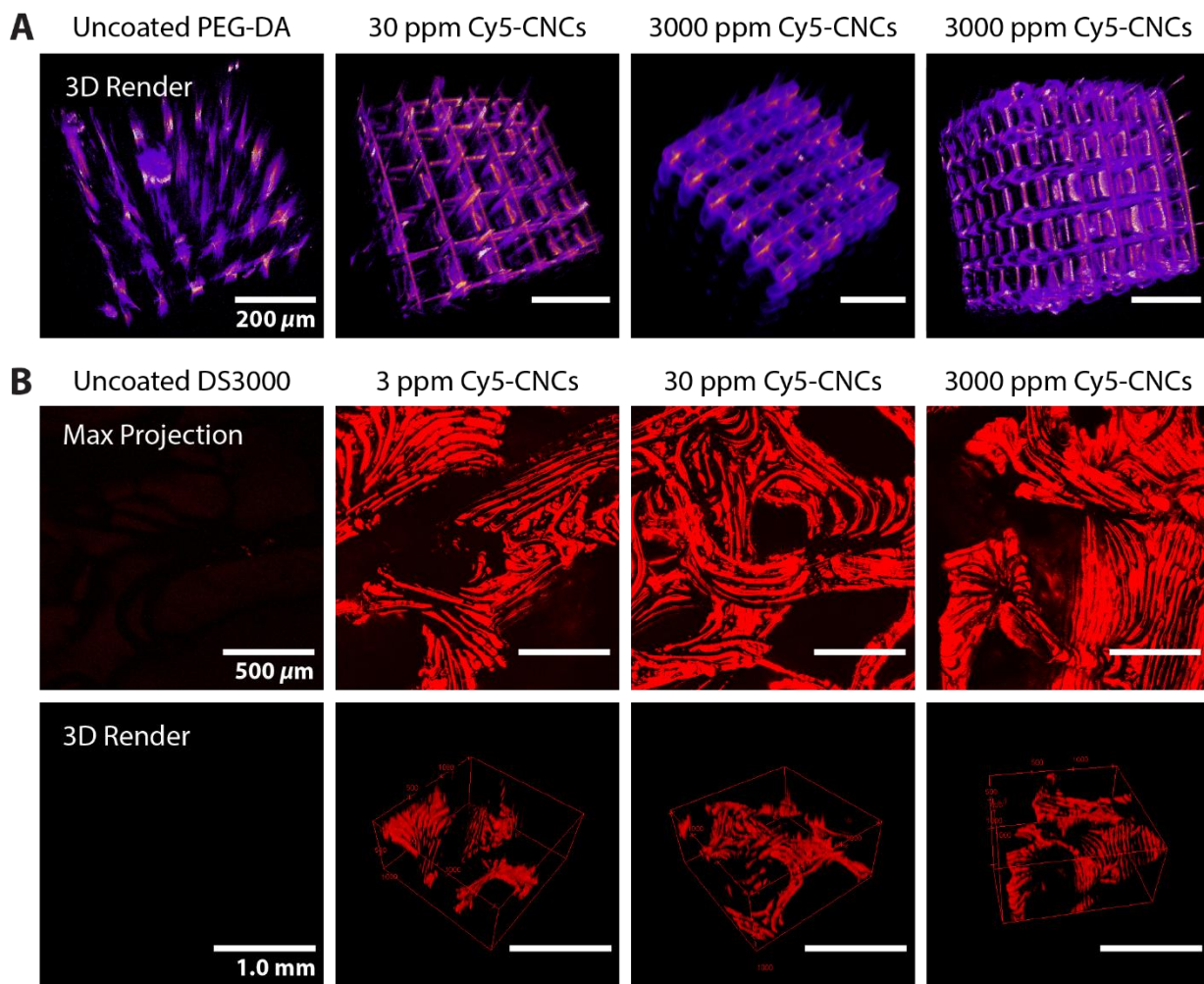


Supplementary Figure 2. The impact of CNC concentration and PAH washing on the surface roughness and nanotopography of coated thin films. **A)** Incomplete washing of excess PAH through a one-step procedure results in the fibrillation of CNCs at coating concentrations higher than 30 ppm. Fibrils begin to form at 300 ppm, and at 3000 ppm the surface is completely covered with highly fibrillated material. As seen in the line height profile of the AFM image, the formation of fibrils introduced large height variations of 10 – 15 nm, as opposed to variations of ~5 nm that are characteristic of individual CNCs and seen in lower CNC coating concentrations. **B)** The removal of excess PAH with two washing steps results in uniform coatings of CNCs at higher concentrations. At a low coating concentration of 3 ppm, the surface is sparsely covered with CNCs and the line height profile occasionally present 5 nm height peaks, causing the RMS roughness to increase from 0.4 nm to 1.1 nm. A 10-fold increase in coating concentrations results in a connected network of CNCs and a significant rise in surface roughness to ~2.1 nm. The coating density continued to increase with higher coating concentrations and the RMS roughness slightly decreases when the surface is completely covered with CNCs when a 3000 ppm CNC solution is used. As seen in the AFM line height profile, complete coverage of the surface with CNCs results in smaller height-to-height variations and in turn a slightly lower RMS roughness compared to surfaces coated with 30 or 300 ppm CNCs which still have some of the thin film surface exposed. **C)** Similar to DS3000 thin films, the surface of PEG-DA thin films can be coated with CNCs to a density that was tuneable by the concentration of CNCs used during the coating process.

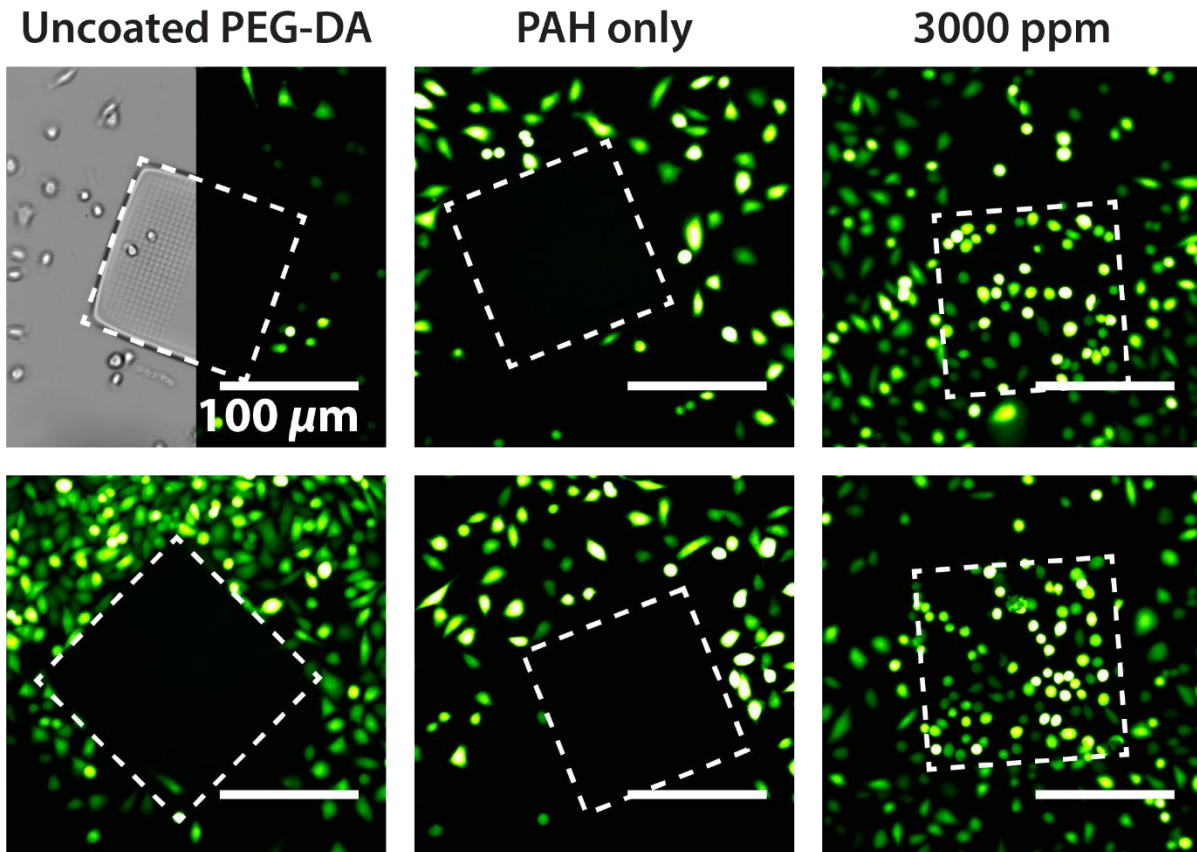


Supplementary Figure 3. The impact of higher order microtopography of 3D-printed surfaces on RMS roughness calculations of CNC coatings. The nanotopography presented by CNC coatings was overlaid on higher order topography of the surface of 3D-printed structures, which arose from “printing lines” during fabrication or structural relaxation after printing. This microtopography was not uniform and significantly impacted the calculated RMS roughness, yielding inconsistent roughness values; to alleviate this, a polynomial background subtraction was performed. Although this allowed extraction of the nanoroughness presented by the CNC coating

and yielded consistent values between different areas of the 3D-printed structure, the RMS roughness of the 3D-printed structures was consistently lower than that of coated thin films (also seen in Figure 3). This discrepancy can be understood by careful analysis of the line height profiles of the coated thin films and the background-subtracted coated 3D-printed surfaces. Due to the flatness of the thin film, the AFM tip was able to probe the full, 5 nm height of the CNCs, while the interference from the high order topography of the 3D-printed surfaces caused the tip to only sense ~2 nm of the CNCs and thus led to lower RMS roughness values.



Supplementary Figure 4. Scanning confocal microscopy images and 3D renderings of 3D DS3000 and PEG-DA structures functionalized with Cy5 using the pre-functionalization approach. **A)** 3D-printed DS3000 trabecular bone model was functionalized with Cy5 by coating the structure with 3, 30 or 3000 ppm CNCs, 10% of which were functionalized with Cy5. A 1.5 x 1.5 x 0.75 mm section was imaged with a 20x/NA0.7 water immersion objective using a Leica SP8 scanning confocal microscope. **B)** The 3D PEG-DA woodpile structures, which were 270 x 270 x 280 μm , were coated and imaged in a similar fashion as the DS3000 structures, and 3D renderings were acquired using the 3D Viewer plugin in ImageJ. The last image is of a structure that was imaged at an angle, which allowed the visualization of the complete 3D-coated structure.



Supplementary Figure 5. The impact of CNC coatings and PAH on the adhesion of PC3-GFP prostate cancer cells to 2.5D PEG-DA pillar arrays. The 3D-printed pillar arrays were either uncoated, coated with PAH only, or with PAH and 3000 ppm CNCs. PC3-GFP cells were seeded at a density of 10,000 cells/cm² for one hour then cultured for 1 day. The cells, which endogenously express GFP in their cytoplasm, were imaged live in the brightfield or green fluorescence channels using a 10x/NA0.3 objective with an Olympus BX51 upright epifluorescence microscope. The pillar arrays were outlined with a dashed white line in the epifluorescence images and highlights how the cells did not bind to the uncoated or PAH-coated structures but completely covered it when densely coated with CNCs.